A high-strength precipitation hardened cobalt-free high-entropy alloy

Matthew Luebbe[1], Jiaqi Duan[1,2,*], Fan Zhang[3], Jonathan Poplawsky[4], Hans Pommeranke[1], Maalavan Arivu[1], Andrew Hoffman[1,5], Mario Buchely[1], Haiming Wen[1,6,*]

[1]Department of Materials Science and Engineering, Missouri University of Science and Technology, Rolla, MO 65409, USA

[2]Warwick Manufacturing Group, University of Warwick, Coventry, CV4 7AL, UK

[3]Materials Measurement Science Division, National Institute of Standards and Technology, Gaithersburg, MD 20899, USA

[4]Center for Nanophase Materials Sciences, Oak Ridge National Laboratory, TN 37996, USA

[5]General Electric Global Research Center, Niskayuna, NY 12309, USA

[6]Department of Nuclear Engineering and Radiation Science, Missouri University of Science and Technology, Rolla, MO 65409, USA

*Corresponding authors: Jiaqi.Duan@warwick.ac.uk, wenha@mst.edu

Abstract

Recent studies on precipitation-hardened high-entropy alloys (HEAs) demonstrate their high strength and thermal stability, making them promising materials for high-temperature structural applications such as nuclear reactors. However, many existing HEAs contain cobalt (Co), which is unsuitable for nuclear applications because of the long-term activation issue of Co. Co is also expensive and considered a critical material for other applications. Therefore, it is desired to exclude Co from the composition. A Co-free $(Fe_{0.3}Ni_{0.3}Mn_{0.3}Cr_{0.1})_{88}Ti_4Al_8$ HEA was developed and studied in this work. In contrast to previous Co-free HEAs, this alloy is close to equiatomic in its composition and promises a more pronounced high-entropy effect. Scanning electron microscopy, transmission electron microscopy, atom probe tomography, and synchrotron-based, high-energy X-ray diffraction were used to characterize this alloy and revealed a complex four-phase structure, with an FCC matrix, γ' precipitates, and a network of B2 and χ phase particles. This structure granted 2151 MPa compressive strength and good thermal stability, but with limited ductility and slow precipitation kinetics. A strengthening analysis of the alloy shows that the B2 and χ provided the most significant strengthening contribution, adding 312 MPa and 788 MPa respectively. The strengthening effect from the small γ′ is also considerable, adding 608 MPa in total. This study lays the foundation for the continued development of high-strength Co-free HEAs with improved and satisfactory ductility.

Keywords

High-entropy alloy; Precipitation Strengthening; Microstructure; Mechanical Properties; Strengthening Mechanisms

1. Introduction

High entropy alloys (HEAs) are alloys with multiple principal elements. They are typically defined as alloys with five or more elements with concentrations from 5 to 35 at % [1-3]. This compositional complexity can lead to severe lattice distortion, reduced diffusion kinetics, and high mixing entropy [1,4]. The existing literature has shown that HEAs possess unique properties, including high solid-solution strengthening, good thermal stability, and good ductility, as well as superior oxidation and wear resistance [5-16]. The high mixing-entropy in HEAs is supposed to promote the formation of a simple single-phase structure instead of intermetallics, and this has been intensively studied in the literature [17-23]. This single-phase (especially face-centered cubic (FCC)) structure may contribute to the high ductility commonly reported in HEAs. Meanwhile, previous studies of solid-solution FCC structured HEAs have shown disappointing strength [23-25].

Recent studies have focused on employing various strengthening mechanisms, especially precipitation strengthening [26-30] to improve the strength of these HEA systems. Through the precipitation of nanostructured phases such as B2, Laves, σ, and carbides, these alloys have shown exceptional strength [9, 31-35]. For example, Gao *et al.* showed a strength increase of 300 MPa by introducing nanoscale NbC to a CrMnFeCoNi alloy [31]. Dasari *et al.* achieved a strength of 1020 MPa with 20 % ductility by engineering B2 precipitation in an $Al_{0.5}Co_{1.5}CrFeNi_{1.5}$ alloy [35]. The most thorough studies have been performed on alloys with an FCC+$L1_2$ (or γ+γ′) structure similar to that observed in Ni-superalloys [26, 28, 30, 36-39]. Two papers by He *et al.* reported a strength of 1100 MPa with a ductility of 40 % for $(FeCoNiCr)_{94}Ti_2Al_4$. They also experimented with other Ti and Al contents but found other compositions impaired either strength or ductility [26, 36]. Yang *et al.* also reported γ′ precipitation in $(CoCrNi)Al_3Ti_3$ with 1300 MPa strength and 45% ductility [38]. These γ′-forming HEAs have exhibited high strength combined with good ductility, but alloy design and processing parameters must be optimized to avoid formation of embrittling intermetallics such as $L2_1$, B2, and σ [37, 40]. Ti and Al are the typical additions to enhance γ′ precipitation in Ni-superalloys and existing HEAs, but they should be added in equal amounts or other Ti and Al containing intermetallics will form [40]. In addition, several papers have shown that γ′ can decay into $L2_1$ or $D0_{24}$ under certain thermo-mechanical processing conditions, impacting the mechanical properties [28, 37].

In addition to increasing strength, precipitates can serve as defect sinks under irradiation, which will improve irradiation resistance [41]. The complex matrix of HEAs also improves their irradiation resistance as shown in Jin *et al.*, in which increasing compositional complexity leads to decreased irradiation-induced swelling [42]. Precipitation-strengthened HEAs are thus expected to have improved irradiation resistance, but most HEAs studied for the irradiation resistance have been single phase [42-47]. Studies performed on irradiation of precipitation strengthened HEAs have focused on the irradiation effects on the precipitates, not the overall alloy [48]. HEAs are also commonly reported to possess good thermal stability which, when combined with good irradiation resistance, makes them promising candidate materials for critical nuclear reactor applications.

Most HEAs reported in the literature, including the high-performance γ+γ′ alloy $(FeCoNiCr)_{94}Ti_2Al_4$, contains Co [1, 26]. Co activates under neutron irradiation with a half-life of

^{60}Co at ≈ 5.27 years, making its presence undesirable for nuclear reactor applications. To address this issue, precipitation hardened HEAs without Co need to be developed for crucial applications in nuclear reactors. Some HEAs without Co have already been developed, including $FeNiMnCr_{18}$ [49], non-equiatomic FeNiMnCrTiAl [27, 50], the FeNiMnAl system [51], $Al_{0.5}Cr_{0.9}FeNi_{2.5}V_{0.2}$ [29, 52], and $Al_{0.3}CrFe_{1.5}MnNi_{0.5}$ [53]. Several systems exhibit excellent mechanical properties and precipitation of phases such as γ′ and B2 [29, 51-54]. However, many of the studied Co-free HEAs, including the best for mechanical properties and precipitation, have compositions that are far from equiatomic, such as $(FeNi)_{67}Cr_{15}Mn_{10}Ti_5Al_3$ or $Al_{0.5}Cr_{0.9}FeNi_{2.5}V_{0.2,}$ potentially impacting its solid-solution strengthening and matrix irradiation resistance [27, 29, 50-53, 55].

According to the original HEA papers, the Cantor alloy, CoCrFeMnNi, forms a stable single-phase FCC alloy and can serve as a good basis for modifying existing compositions [3,4]. The goal of the current study was to develop an FCC+γ′ HEA without Co for nuclear applications. To achieve this goal, the existing and well-studied $(FeCoNiCr)_{94}Ti_2Al_4$ alloy was used as a basis and the Co was replaced with Mn based on the Cantor alloy. Due to the tendency of Cr to form intermetallics, especially with Mn, the concentration of Cr is also reduced, and the Ti and Al contents were increased to allow more formation of $Ni_3(Ti,Al)$ γ′ precipitates. The alloy developed and tested in this study is much closer to an equiatomic HEA than previous Co-free HEAs, leading to better overall HEA character.

2. Experimental Procedures

Bulk $Fe_{26.4}Ni_{26.4}Mn_{26.4}Cr_{8.8}Ti_4Al_8$ [or $(Fe_{0.3}Ni_{0.3}Mn_{0.3}Cr_{0.1})_{88}Ti_4Al_8$] HEA samples were fabricated by vacuum induction melting of 99.9 % pure elemental material. X-ray fluorescence (XRF) was performed on samples from the cast to ensure they matched the composition, with the results shown in Table 1. To ensure compositional homogeneity and a starting single-phase FCC structure, the cast was homogenized at 1100 °C for 48 h in an air-filled SiC furnace inside carbon filled stainless steel bags to limit oxidation. The oxide layer which formed was removed prior to aging. The homogenized sample was then sectioned and aged at 650 °C for varying durations from 0.5 h to 244 h in a box furnace. The samples were mechanically polished with a final step of 0.02 μm colloidal silica for subsequent characterization.

Table 1: Elemental composition of the overall alloy as determined by XRF compared to the nominal composition. All compositions are in atomic percent.

	Fe	Ni	Mn	Cr	Ti	Al
Nominal	26.4	26.4	26.4	8.8	4	8
Experimental	26.6 ± 0.2	27.3 ± 2.1	25.3 ± 2.6	8.5 ± 0.1	4.2 ± 0.1	8.1 ± 0.7

In this study, the microstructure characterization of the homogenized and peak aged samples was performed using electron backscatter diffraction (EBSD), energy dispersive spectroscopy (EDS), transmission electron microscopy (TEM), scanning transmission electron microscopy (STEM) and atom probe tomography (APT). EBSD and EDS were performed using a

Helios Dual-Beam Nanolab* scanning electron microscope (SEM) operated at 30 kV, with a step size of 200 nm and 50 nm for the EBSD scans in Figures 1 and 9, respectively. TEM samples were prepared using focused ion beam (FIB) lift-out on the Helios and (S)TEM characterization was performed using an FEI F20 TEM at 200 kV. The FIB on the Helios SEM was also used to mill, lift out, and thin APT tips as described by Thompson *et al.* [56]. APT experiments were performed using a CAMECA local electrode atom probe (LEAP 4000XHR) in laser mode with a 30K base temperature and a 50 pJ laser energy. Reconstructions were created and analyzed using CAMECA's IVAS 3.8 software.

The bulk microstructure of the alloys was also characterized using synchrotron-based X-ray diffraction measurements in transmission mode. The measurements were conducted at 9-ID-C and 11-ID of the Advanced Photon Source, Argonne National Laboratory. The X-ray wavelength was 0.5904 Å for 9-ID and 0.2113 Å for 11-ID, respectively. The photon flux at the sample was ~ 10^{13} photon/mm^2/s. X-ray beam size was 800 μm × 200 μm (9-ID) and 200 μm × 200 μm (11-ID), respectively. More details about the instruments can be found elsewhere. [57, 58].

Hardness testing was performed using a Struers Duramin 5 Vickers hardness tester by applying a load of 4.91 N for a duration of 10 s. Tensile testing was performed using an MTS Landmark materials testing system with a 250 kN load cell. The homogenized sample was machined into tensile specimens with dimensions of 23 mm gauge length × 6.2 mm width × 5.8 mm thickness using electric discharge machining (EDM) equipment with a brass wire. The peak-aged samples proved too brittle for tensile testing and were cut into compression specimens with dimensions of 6.8 mm height × 6.4 mm × 5.8 mm cross-section. The displacement rates for tensile and compressive testing were 1.4 mm/min and 0.032 mm/min, respectively.

A CALPHAD (Calculation of Phase Diagrams) approach was used to predict and evaluate phases and their chemical compositions in the $(Fe_{0.3}Ni_{0.3}Mn_{0.3}Cr_{0.1})_{88}Ti_4Al_8$ HEA. Equilibrium CALPHAD calculations were performed using Thermo-Calc software, with a HEA database (TCHEA4). This HEA database is based on binary and ternary subsystems and the model predictions are their extrapolations for a given composition.

3. Results

3.1. Heat Treatment

The as-cast alloy was first homogenized at 1100 °C for 48 h to ensure compositional homogeneity. To confirm that the pre-aged sample was FCC structured single-phase with no compositional variation, we used local probes such as EDS, EBSD, and APT as well as the bulk probe of synchrotron XRD on the homogenized sample. The secondary electron SEM image in Figure 1a shows some areas that appear to be secondary phases, but the EBSD phase map, as shown in Figure 1b, suggests that the homogenized sample is an FCC single-phase within its

* Certain commercial products or company names are identified here to describe our study adequately. Such identification is not intended to imply recommendation or endorsement by the National Institute of Standards and Technology, nor is it intended to imply that the products or names identified are necessarily the best available for the purpose.

detection limit. The unindexed region in Figure 1b represents TiN inclusions according to EDS taken with the map, and the overall volume fraction of the inclusions is negligible. To eliminate the possibility of misindexing by the software, Figure 1c and 1d show a Kikuchi pattern collected during the EBSD mapping, and its match after indexing respectively. Overall the indexed pattern corresponds to that of FCC iron. The atom maps also show that, within the analyzed volume, the matrix is compositionally homogeneous. The XRD data, serving as a bulk probe, indicate a dominant FCC diffraction pattern with a lattice constant of (3.640 ± 0.002) Å, shown in Figure 2. For completeness, we note that a weak peak exists on the right shoulder of the FCC 111 peak, indicating the possibility of a secondary phase. We emphasize that this peak is the only peak detected for a possible secondary phase even with the high X-ray flux in a synchrotron measurement, and its integrated intensity is less than 1% of that of the FCC 111 peak, proving the bulk evidence that the homogenized material is effectively a single-phase FCC alloy.

An aging study was performed to examine the evolution of material hardness as a function of aging duration and temperature. Aging temperatures which were tested are shown in Table 2, along with max hardness achieved and additional characterization performed. We experimentally determined that aging at 650 °C for 120 h represents the optimal aging condition leading to the highest strength (hardness). The hardness data after aging at 550 °C, 650 °C, and 800 °C for various duration, as shown in Figure 3, demonstrate a wide range of materials' responses to heat treatment conditions near the optimal temperature of 650 °C.

Table 2: Aging temperatures performed in the aging study, with maximum duration, hardness and additional characterization performed listed

Aging Temperature	Max Duration	Max Hardness	Characterization
550 C	120 h	266 HV	APT
600 C	72 h	452 HV	None
650 C	244 h	535 HV	APT, SEM, TEM
700 C	72 h	391 HV	None
750 C	48 h	310 HV	None
800 C	120 h	306 HV	APT, SEM

The as-homogenized material has a Vickers hardness of 151 HV. At 650 °C, the hardness increases rapidly to 432 HV after an aging time of 24 h. It continues to increase until 120 h of aging to a peak hardness of 535 HV. The hardness remains relatively stable, indicating that the precipitates and other phases that lead to improved hardness are thermally stable at this temperature. The slight downward trend may be related to a slow coarsening process.

At 550 °C, the hardness value increases quickly and then the rate of increase slows down. After 120 h of heat treatment at 550 °C, the material achieved a hardness of 266 HV. At 800 °C, the Vickers hardness increases rapidly to 306 HV after 12 h, at which point the hardness quickly decreases until reaching a stable value of ≈ 270 HV after ≈ 50 h. These hardness data unequivocally demonstrated that 650 °C is preferred for age hardening.

3.2. Mechanical Properties

The $(Fe_{0.3}Ni_{0.3}Mn_{0.3}Cr_{0.1})_{88}Ti_4Al_8$ was mechanically tested in both the homogenized and peak-aged condition, as shown in Figure 4. In the homogenized condition, the alloy has a yield strength of 375 MPa, an ultimate tensile strength of 746 MPa, and an elongation of 18% before failure. When aged at 650 °C for 120 h, the peak-aged alloy was too brittle for effective tensile measurements. Compression testing of pieces taken from the tensile bars was performed to evaluate the alloy strength. The sample exhibited a yield strength of 1800 MPa and an ultimate compressive strength of 2151 MPa, slightly exceeding the recorded hardness of 535 HV≈1750 MPa, but the compressive ductility was only (3.8 ± 0.1) %.

3.3. Microstructure after aging

3.3.1 Characterization of precipitates using EDS in SEM and TEM

We characterized the peak-aged alloy using EDS in both the SEM and TEM. A complicated microstructure of an FCC matrix and two other precipitating phases with elemental segregation were observed, as shown by the SEM data in Fig. 5. The first phase is a NiAl-enriched and FeCr-depleted B2 phase which appears lighter than the matrix under secondary electron SEM imaging. The second phase is an FeCr-enriched and NiAl-depleted χ (or Chi) phase that appears both darker than the matrix and slightly upraised from the matrix, indicating that it has a higher abrasion resistance to mechanical polishing. Notably, these two phases grow adjacent to each other in a network structure. Examples of the two phases are labeled in Figure 5a and 5c-f. TEM data support these SEM findings, as shown in Fig. 6. The higher resolution of TEM enables elemental distribution to be more clearly observed than SEM. Specifically, while Mn appears to be homogeneous under SEM, TEM data demonstrated a slight preference for B2. Ti, which appears to be enriched in both B2 and χ under SEM, appears to show a slight preference for χ instead of B2 at a smaller scale.

Besides the B2 and χ phases, Ni_3(Ti, Al) type $L1_2$ (γ′) precipitates were also observed in the FCC matrix using APT (shown later). However, they are too small for observation in SEM, and difficult to pinpoint alongside the B2 and χ phases in TEM.

3.3.2. Crystal structure and phase confirmation via diffraction techniques

To conclude that the NiAl and FeCr enriched phases were indeed B2 and χ, respectively, these phases in a peak aged sample (650 °C for 120 h) were characterized using bright-field imaging and selected-area electron diffraction (SAED) in TEM, as shown in Figure 7. The NiAl-rich particle shown in Figure 7b-c exhibits superstructure in the lattice expected for B2. The lattice parameter derived from the SAED pattern is 3.00 ± 0.04 Å, similar to the 2.91 Å reported in the literature for NiAl-type B2 phases [59]. In addition, the B2 phase contains a stacking structure, visible in Figure 7a and b. This structure does not involve compositional variation, as shown in Figure 6, and could originate from twinning previously observed in the B2 phases [60]. Figure 7d-e shows a FeCr-rich phase particle along with its SAED pattern, indexing it as χ phase. This phase is an ordered version of α-Mn and has a lattice parameter of 8.83 ± 0.26 Å, similar to the 8.89 Å value reported for other χ-phases in the literature [61]. We also used synchrotron-based XRD to analyze the bulk structure of the alloy. The results are shown in Figure 8. The presence of FCC (lattice parameter of a=3.638 ± 0.002 Å), B2 (lattice parameter of a=2.922 ± 0.002 Å), and χ

(lattice parameter of a=8.892 ± 0.006 Å) was confirmed based on XRD. The lattice parameters of each phase are very similar to those recorded in the literature but different (2.3% and 0.6% for B2 and χ, respectively) from those measured from TEM. The difference most likely originates from the calibration and collimation conditions of the TEM, and we regard the X-ray results as more accurate. Using the crystallographic information of the matrix and precipitates as input, we performed EBSD to acquire an improved understanding of the morphology and microstructure of these phases. EBSD measurements, shown in Figure 9 demonstrate that the NiAl-rich phase is indexed as B2 phase and the FeCr indexed as χ, consistent with the TEM findings in Figure 7.

3.3.3. Nanoscale characterization of precipitates using APT

We characterized the morphology and chemical composition of the precipitates using APT to take advantage of its sub-nm spatial resolution. Two examples, both acquired using peak-aged materials, are shown in Figs. 10-12 to highlight different phases. The APT reconstruction in Fig. 10 reveals nano-scale precipitates with diameters of about 20 nm distributed throughout the FCC matrix. These precipitates were delineated using a 40 at.% Ni iso-concentration surface (isosurface). The 3D concentration profiles across the matrix/precipitates interface indicate that the precipitates are rich in Ni and Ti, as expected for the γ' phase. An Al-rich precipitate is also present at the top of the APT tip, and the proximity histogram (proxigram) concentration profiles in Figure 11b indicate that this precipitate is B2. A second APT reconstruction in Figure 12 shows a χ particle rich in Fe and Cr. In addition, Figure 12b confirms the observation from Figure 5g that both B2 and χ phases are enriched in Ti. Table 3 summarizes the composition of each phase, from the APT analysis for $(Fe_{0.3}Ni_{0.3}Mn_{0.3}Cr_{0.1})_{88}Ti_4Al_8$ aged at 650 °C for 120 h. Overall the quantitative compositions determined by APT closely match the qualitative observations obtained from SEM and STEM EDS.

Table 3: Elemental composition for each of the four phases in $(Fe_{0.3}Ni_{0.3}Mn_{0.3}Cr_{0.1})_{88}Ti_4Al_8$ aged at 650 °C for 120 h as determined by APT. All concentrations are in atomic percent. Composition uncertainties were less than 0.1 at.% for FCC and γ′, and less than 0.5 at.% for χ and B2.

Phase	Fe	Ni	Mn	Cr	Ti	Al
FCC (γ)	36.1	22.3	28.7	10.3	1.6	1.0
γ′	1.9	70.0	2.5	0.2	21.1	4.3
B2	4	45	31.5	0.5	5	14
χ	45.5	5.5	25.5	18.5	4.5	0.5

3.4. CALPHAD modeling

We used Thermo-Calc modeling with the TCHEA3 database to predict phases and their compositions. Figure 13 shows the equilibrium phase diagram for our chosen HEA composition within a temperature range of 0 °C to 1600 °C. The predicted compositions of the thermodynamic equilibrium phases are provided in Table 4. Among these compositions, the predicted compositions of γ′ (modeled as Ni_3Ti in the database) and B2 are similar to our experimental

values. The model predicts a FeCr-rich σ phase without Ti or Al. Experimentally, we observed a FeCr-rich χ phase with ≈ 5 at. % Ti. We attribute this critical inconsistency between the model and experiment to the incompleteness (missing χ phase) and the extrapolation of the HEA database. We also note that besides the misprediction of the σ phase, our CALPHAD model also predicted the formation of several lower temperature phases and the disappearance of the FCC matrix, neither of which occurs experimentally. However, because the equilibrium phase diagram only concerns the equilibrium phases, we must consider the possibility that the necessary kinetic time scale for these phenomena to happen may be outside our measurement window.

Table 4: Thermo-Calc predicted equilibrium composition and phase volume percentages at the 650 °C isotherm. All compositions are in atomic percent.

Phase	Fe	Ni	Mn	Cr	Ti	Al	Volume percent
FCC	46.3	20.8	26.3	3.0	0.4	3.2	18.7%
Ni_3Ti/γ'	23.5	51.5	0	0	24.3	0.7	16.0%
B2	7.2	45.6	23.2	0.3	0.5	23.2	32.0%
σ	34.6	0.5	41.2	23.7	0	0	33.3%

4. Discussion

4.1. Precipitate morphology and formation

Our work demonstrated that the homogenized alloy has a primary FCC structure. The peak-aging heat treatment (650 °C for 120 h) promoted the formation of several types of precipitates, namely, B2, χ, and γ′. We generally observed slow precipitation and coarsening kinetics in this alloy, because of the HEA's slow atomic diffusion. For example, at 800 °C, this alloy reached its peak hardness after 12 h. In comparison, Haynes 282 [65], a commercial Ni-based superalloy, experiences nucleation, growth, and coarsening within 4 h at 800 °C, and other common alloys also exhibit faster precipitation kinetics [62-65].

The size, morphology, and volume fraction of the γ' in $(Fe_{0.3}Ni_{0.3}Mn_{0.3}Cr_{0.1})_{88}Ti_4Al_8$ are similar to some HEA systems reported in the literature; for example, $(FeCoNiCr)_{94}Ti_2Al_4$ from He *et al.* [26] exhibited 12.6 nm particle radius and 23 vol%, greater than the 11.0 nm and 10 vol% observed in this work. Our observation of the B2 and χ is similar to those reported by Chen *et al.* [40]. Using a composition $CoCrFeNi(Ti_xAl_y)_{0.2}$, which is similar to the alloy in this study, Chen et al systematically investigate the effect of varying amounts of Ti and Al on the precipitated phases. They concluded that an equiatomic amount of Ti and Al favors optimal strengthening from the γ′ phase, and also suggested that excess Ti encourages the formation of η phases, σ phases, and Laves phase. In contrast, excess Al encourages the formation of B2 and σ phases. The alloy in this study is Al-rich, and we found the formation of B2 and χ consistent with Chen *et al.*'s findings.

The extensive network morphology of the B2 and χ secondary phases is unexpected. To our knowledge, neither Ni-superalloys nor aged HEAs have shown this type of morphology under aging conditions. Both B2 and χ phase give rise to high strength and poor ductility, contributing

to this alloy's brittle nature. The interconnected morphology of these two phases suggests co-precipitation, spinodal decomposition, or a precipitation reaction [66, 67]. For example, spinodal decomposition can present a similar morphology, but its occurrence typically requires compositional microsegregation along the grain boundaries or near the interdendritic regions [68, 69]. In the case of spinodal decomposition, the neighboring phases usually have similar atomic structures, such as FCC/γ′ and BCC/B2 [29, 70]. The appearance of the precipitates could also indicate how they formed. In this study, the B2 phase exhibits nanoscale linear/stacking structures under TEM with no apparent elemental segregation. This feature was previously been attributed to nanotwins [60, 71]. The combined phase morphology of the B2 and χ resembles a B2 matrix with χ particles, suggesting a precipitate reaction similar to that observed in duplex stainless steels in which a ferrite phase (or B2) decomposes into the austenite and σ phase [72-75]. However, the existing TEM characterization does not show the chemistry variation along the B2 banded structure expected for this decomposition theory, and therefore further characterization is required.

In addition, the formation of χ phase instead of the CALPHAD predicted σ phase is noteworthy. This difference may be due to lack of the thermodynamic description for χ phases within the CALPHAD database due to their rarity. Specifically, the CALPHAD model for χ phase excludes Co and Mn from the phase, but our extensive literature review leads to one paper reporting a χ phase formation in HEAs, with a χ-phase matrix observed in the Co-containing $Al_{0.25}Ti_{0.75}CoCrFeNi$ HEA [76]. The χ phase is often reported in Mo-containing stainless steels, especially duplex stainless steels [77-80]. The detrimental χ phase typically forms along grain boundaries within these steels, leading to lower ductility and corrosion resistance [80]. Some papers on the χ phase in steels have suggested that it is a metastable phase that eventually transforms into the σ phase [81, 82]. If such a transformation occurs in HEAs, it may contribute to the discrepancy between our experimental data and CALPHAD predictions. In this alloy, however, the χ phase is stable at 650 °C for at least 120 hours, highlighting the stability of this phase. While we cannot conclusively suggest that the χ phase is an equilibrium phase, its long-term stability has significance regarding an improved database evaluation. We also point out that recent studies have suggested that the σ phase may not be thermodynamically favorable compared to other intermetallics [83], creating an alternative explanation that the χ phase may be the equilibrium phase for our experimental conditions. A longer-duration heat treatment study is warranted to test this hypothesis.

4.2. Strengthening analysis

We analyzed the SEM/EBSD images and APT reconstruction data to determine the characteristics of each phase in the $(Fe_{0.3}Ni_{0.3}Mn_{0.3}Cr_{0.1})_{88}Ti_4Al_8$ aged at 650 °C for 120 h. The results, including the size, number density and volume %, are shown in Table 5. We obtained the volume and area-equivalent diameters for these phases using the average volume for γ′ and the average area for B2 and χ. We then used these sizes as input parameters for their appropriate strengthening models to evaluate each phase's strengthening effect.

For the γ′ phase, we analyzed their precipitate shearing and Orowan looping to determine the operative mechanism. In the case of B2 and χ, whose sizes, morphology and distribution do not lead to the precipitate shearing or Orowan looping, a load-transfer mechanism was used for

strengthening analysis with an FCC matrix phase. A summary of the results from the strengthening analysis is presented in Figure 14. The predicted yield strength, with combined strengthening from all precipitates, is 1892 MPa, slightly more than the measured value of 1800 MPa but within the uncertainties of the measurements used for calculations. The detailed analysis is described below.

Table 5: Characteristics of the four phases in the system, with size, number density and volume percent determined from SEM/EBSD for B2 and χ and from APT for γ'

Phase	Average Size (nm)	Number Density (/m^3)	Volume (%)
FCC	N/A	N/A	38.83 ± 6.81
γ'	22.1 ± 3.6	3.65 ± 0.49E22	10.08 ± 1.77
B2	330 ± 56	1.93 ± 0.66E12	28.95 ± 3.19
χ	360 ± 72	1.14 ± 0.29E12	22.14 ± 5.39

Due to the prolonged homogenization heat treatment, the grain size grew to hundreds of micrometers. A low dislocation density is expected due to the homogenization and aging heat treatments. Hence, grain boundary and dislocation strengthening were ignored in our consideration.

For the γ' phase, strengthening contribution from the Orowan looping mechanism is given by [84]

$$\Delta\sigma_{or} = M\frac{0.4Gb}{\pi\lambda}\frac{\ln(2\bar{r}/b)}{\sqrt{1-\nu}} \quad (1)$$

Where M = 3.06 is the mean orientation factor for polycrystalline FCC, G is the shear modulus of the matrix, 78.5 GPa [26], $b = \sqrt{2}/2a$ is the Burgers vector magnitude, 0.257 nm, $\bar{r} = \sqrt{\frac{2}{3}}r = 9.02$ nm is the mean radius of circular cross-section through the spherical precipitate, ν is the Poisson's ratio, 0.31 [36], and λ is the precipitate spacing, given by

$$\lambda = 2\bar{r}\left(\sqrt{\frac{\pi}{4f}} - 1\right) = 32.32\ nm \quad (2)$$

Where f is the volume fraction of $L1_2$ precipitates, 10.08%. The total strengthening from the precipitates is 1.24 GPa in the FCC region.

Given the high strengthening predicted by the Orowan looping mechanism, the precipitate shearing mechanism is also considered to determine whether the looping mechanism or the shearing mechanism is active. Precipitate strengthening occurs by either a shearing or looping mechanism: the one leading to a smaller strength increment is the operative mechanism. In the case of the shearing mechanism, the total strengthening contribution is taken as the larger of $\Delta\sigma_{cs} + \Delta\sigma_{ms}$ and $\Delta\sigma_{os}$, where $\Delta\sigma_{cs}$ is the matrix-precipitate coherency strengthening, $\Delta\sigma_{ms}$ is the modulus mismatch strengthening, and $\Delta\sigma_{os}$ is the order strengthening. Each strengthening contribution is calculated below: [26, 85]

$$\Delta\sigma_{cs} = M * \alpha_e * (G * \varepsilon)^{3/2}\left(\frac{rf}{0.5Gb}\right)^{1/2} \quad (3)$$

$$\Delta\sigma_{ms} = 0.0055 * M * (\Delta G)^{3/2}\left(\frac{2f}{G}\right)^{1/2}\left(\frac{r}{b}\right)^{\frac{3m}{2}-1} \quad (4)$$

$$\Delta\sigma_{os} = 0.81 * M * \left(\frac{\gamma_{APB}}{2b}\right)\left(\frac{3\pi f}{8}\right)^{1/2} \quad (5)$$

Where M = 3.06, α_e = 2.6, m = 0.85, the matrix modulus $G = G_m$ =78.5 GPa [26], the precipitate modulus G_p = 77.4 GPa [86], $\Delta G = G_m - G_p$ = 1.1 GPa, r is the average precipitate radius, 11.05 nm, f is the volume fraction of $L1_2$ precipitates, 0.1008, b is the Burger's vector, 0.257 nm, γ_{APB} is the APB energy for γ' particles, 0.12 J/m^2 [87], and $\varepsilon = \frac{2}{3}\left(\frac{\Delta a}{a}\right)$ is the constrained lattice parameter, 0.0141, using a matrix lattice parameter of a_m=0.3638 nm and a precipitate lattice parameter of a_p=0.3561 nm. The contributions from each strengthening mechanism are $\Delta\sigma_{cs} = 3.1\ GPa$, $\Delta\sigma_{ms} = 2.77\ MPa$, and $\Delta\sigma_{os} = 199\ MPa$. Because $\Delta\sigma_{or}(1.24\ GPa) < \Delta\sigma_{cs} + \Delta\sigma_{ms}$ $(3.1\ GPa)$, the operative mechanism for γ' precipitate strengthening is the Orowan looping mechanism, with a strengthening contribution of 1.24 GPa in the FCC region. As the FCC region makes up only 48.91% of the alloy, the overall contribution of γ′ in the alloy is 608 MPa.

For some HEAs (especially those that are single-phase solid solutions), a significant source of strengthening comes from solid solution strengthening. However, most existing solid solution strengthening models require one or two elements to serve as a solvent for the rest. Given the complexity of HEAs, there is no conventional solvent element, so most existing models do not apply. We estimated this effect by assuming that the homogenized sample has the same solid-solution strengthening as the FCC phase of the aged sample, and that it is the only strengthening mechanism in operation for the homogenized samples. Thus, the solid-solution strengthening can be estimated as $\Delta\sigma_{ss} = \sigma_{hom} - \sigma_0$, where σ_0 is the base strength, taken as the yield strength 265 MPa for the TiAl-free base FCC HEA, $FeNiMnCr_{10}$ [88], and σ_{hom} is the observed yield strength for the homogenized sample in Figure 4. Under this assumption, the solid solution strengthening from alloying additions is estimated at 110 MPa.

For B2 and χ phases, the precipitate sizes are relatively large, and their combined morphology makes it more realistic to consider them separate phases from the FCC matrix rather than a precipitate phase within the matrix for which Equations 1 and 2 are viable. Thus, their strengthening contributions are determined by the load transfer mechanism, often expressed by the rule of mixtures, given as

$$\sigma_{alloy} = f_{FCC+\gamma'}\sigma_{FCC+\gamma'} + f_{B2}\sigma_{B2} + f_{\chi}\sigma_{\chi} \quad (6)$$

Where f_i, with i=FCC+γ′, B2, or χ, is the volume fraction of the phase and σ_i is the strength of the phase as determined from the literature. The strengths of the phases are taken as $\sigma_{FCC+\gamma'} = 1619$ MPa, considering precipitate and solid solution strengthening from this work, and the literature, $\sigma_{B2} = 1078$ MPa, and $\sigma_{Chi} = 3561$ MPa [75, 88, 89]. For this equation, $f_{FCC+\gamma'}$ is taken to be 48.91%, including both FCC and γ'. The total strengthening from B2 and χ are 312 MPa and 788 MPa, respectively, as shown graphically in Figure 14. Overall, the most significant contribution to

the strength was the B2 and χ precipitates, which led to low ductility in the peak-aged condition, but the γ′ precipitates also made a significant contribution to the strength. Future work is needed to optimize the composition and heat treatment protocol to control the formation of these intermetallic phases. In addition, the compositional complexity of the intermetallics may have led to solid solution strengthening to the intermetallics which were not accounted for when using the strength values of B2 and χ from the literature in the Equation 6 calculations.

5. Conclusions

We fabricated a high strength Co-free $(FeNiMnCr_{10})_{94}Ti_2Al_4$ alloy through casting and heat treatments. A systematic aging analysis reveals a peak aging condition of 650 °C for 120 h. A comprehensive microstructural analysis of the peak aged specimens, coupled with CALPHAD prediction and strengthening calculations, indicates that precipitation of several intermetallic phases is responsible for the high strength of the peak aged alloy. The main conclusions of the study are:

1. When aged at 650 °C the alloy exhibited exceptional mechanical properties, peaking at 535 HV or an equivalent yield strength of 1750 MPa. The peak aged alloy had no tensile ductility and compressive testing indicated a yield strength of 1.8 GPa and an ultimate compressive strength of 2.15 GPa. The HEA also exhibits excellent thermal stability at 650 °C, with the hardness only decreasing by 30 HV after aging for an additional 120 after passing the peak-aging condition.
2. The microstructure of the HEA was not the typical FCC+γ' structure. Instead, it exhibited a B2+χ phase structure alongside the FCC+γ′. This structure is enriched in Ti overall, with Ni and Al enriched B2 and Fe and Cr enriched χ phase. Overall, the B2+χ structure makes up >50% of the total volume.
3. Results from a strengthening analysis closely match the observed compressive yield strength, (1800 MPa). The most considerable strengthening component (1100 MPa total) originates from the B2/χ structure, while also contributing to the alloy's brittle nature. The γ′ contributes to the strength as well with 608 MPa.
4. CALPHAD modeling of this alloy predicts B2 and σ phase forming in addition to γ', while χ phase was observed instead of σ. This discrepancy may be due to the incompleteness of the thermodynamics description of the HEA database, and our results provide the needed datapoints to improve the database.

ACKNOWLEDGEMENTS

This research was partially financially supported by the U.S. Nuclear Regulatory Commission Faculty Development Program (award number NRC 31310018M0044). This research used resources of the Advanced Photon Source, a U.S. Department of Energy (DOE) Office of Science user facility operated for the DOE Office of Science by Argonne National Laboratory under Contract No. DE-AC02-06CH11357. APT research was supported by the Center for Nanophase Materials Sciences (CNMS), which is a US Department of Energy, Office of Science User Facility at Oak Ridge National Laboratory. The authors would like to thank James Burns for assistance in performing APT sample preparation and running the APT experiments.

References

[1] Miracle, D.B., Senkov, O.N. (2017). A critical review of high entropy alloys and related concepts. *Acta Materialia, 122,* 448-511.

[2] Tsai, M.-H., Yeh, J.-W. (2014). High-Entropy Alloys: A Critical Review. *Materials Research Letters, 2*(3), 107-123.

[3] Cantor, B., Chang, I., Knight, P., & Vincent, A. (2004). Microstructural development in equiatomic multicomponent alloys. *Materials Science and Engineering: A*, *375-377*, 213–218.

[4] Yeh, J.-W., Chen, S.-K., Lin, S.-J., Gan, J.-Y., Chin, T.-S., Shun, T.-T., … Chang, S.-Y. (2004). Nanostructured High-Entropy Alloys with Multiple Principal Elements: Novel Alloy Design Concepts and Outcomes. *Advanced Engineering Materials*, *6*(5), 299–303.

[5] George, E.P., Curtin, W.A., Tasan, C.C. (2020). High entropy alloys: A focused review of mechanical properties and deformation mechanisms. *Acta Materialia, 188,* 435-474.

[6] Wang, X.F., Zhang, Y., Qiao, Y., Chen, G.L. (2007). Novel microstructure and properties of multicomponent CoCrCuFeNiTi_x alloys. *Intermetallics, 15,* 357-362.

[7] Fu, Z., Chen, W., Wen, H., Zhang, D., Chen, Z., Zheng, B., Zhou, Y., Lavernia, E.J. (2016). Microstructure and strengthening mechanisms in an FCC structured single-phase nanocrystalline $Co_{25}Ni_{25}Fe_{25}Al_{7.5}Cu_{17.5}$ high-entropy alloy. *Acta Materialia, 107,* 59-71.

[8] Chen, J., Zhou, X., Wang, W., Liu, B., Lu, Y., Yang, W., Xu, D., Liu, Y. (2018). A review on fundamentals of high entropy alloys with promising high-temperature properties. *Journal of Alloys and Compounds, 760,* 15-30.

[9] Ma, Y., Hao, J., Jie, J., Wang, Q., Dong, C. (2019). Coherent precipitation and strengthening in a dual-phase $AlNi_2Co_2Fe_{1.5}Cr_{1.5}$ high-entropy alloy. *Materials Science and Engineering A, 764,* 138241.

[10] Bai, X., Fang, W., Chang, R., Yu, H., Zhang, X., Yin, F. (2019). Effects of Al and Ti additions on precipitation behavior and mechanical properties of $Co_{35}Cr_{25}Fe_{40-x}Ni_x$ TRIP high entropy alloys. *Materials Science and Engineering A, 767,* 138403.

[11] Liu, Y.Y, Chen, Z., Chen, Y.Z., Shi, J.C., Wang, Z.Y., Wang, S., Liu, F. (2019). Effect of Al content on high temperature oxidation of $Al_xCoCrCuFeNi$ high entropy alloys (x=0, 0.5, 1, 1.5, 2). *Vacuum, 169,* 108837.

[12] Li, T., Swanson, O.J., Frankel, G.S., Gerard, A.Y., Lu, P., Saal, J.E., Scully, J.R. (2019). Localized corrosion behavior of a single-phase non-equimolar high entropy alloy. *Electrochimica Acta, 306,* 71-84.

[13] Zhang, H.X., Dai, J.J., Sun, C.X., Li, S.Y. (2020). Microstructure and wear resistance of TiAlNiSiV high-entropy laser cladding coating on Ti-6Al-4V. *Journal of Materials Processing Technology, 282,* 116671.

[14] Wang, J., Zhang, B., Yu, Y., Zhang, Z., Zhu, S., Lou, X., Wang, Z. (2020). Study of high temperature friction and wear performance of $(CoCrFeMnNi)_{85}Ti_{15}$ high-entropy alloy coating prepared by plasma cladding. *Surface and Coatings Technology, 384,* 125337.

[15] Soni, V.K., Sanyal, S., Sinha, S.K. (2020). Phase evolution and mechanical properties of novel FeCoNiCuMox high entropy alloys. *Vacuum, 174,* 109173.

[16] Zhao, S. (2019). Defect properties in a VTaCrW equiatomic high entropy alloy (HEA) with the body centered cubic (bcc) structure. *Journal of Materials Science and Technology, 44,* 133-139.

[17] Otto, F., Yang, Y., Bei, H., George, E.P. (2013). Relative effects of enthalpy and entropy on the phase stability of equiatomic high-entropy alloys. *Acta Materialia, 61,* 2628-2638.

[18] Zhang, F., Zhang, C., Chen, S.L., Zhu, J., Cao, W.S., Kattner, U.R. (2014). An understanding of high entropy alloys from phase diagram calculations. *CALPHAD, 45,* 1-10.

[19] Kim, D.G., Jo, Y.H., Park, J.M., Choi, W.-M., Kim, H.S., Lee, B.-J., Sohn, S.S., Lee, S. (2020). Effects of annealing temperature on microstructure and tensile properties of a single FCC phase CoCuMnNi high-entropy alloy. *Journal of Alloys and Compounds, 812,* 152111.

[20] Qi, J., Cheung, A.M., Poon, S.J. (2019). High entropy alloys mined from binary phase diagrams. *Scientific Reports, 9,* 15501.

[21] Zhang, T., Xin, L., Wu, F., Zhao, R., Xiang, J., Chen, M., Jiang, S., Huang, Y., Chen, S. (2019). Microstructure and mechanical properties of FexCoCrNiMn high-entropy alloys. *Journal of Materials Science and Technology, 35*(10), 2331-2335.

[22] Yang, S., Lu, J., Xing, F., Zhang, L., Zhong, Y. (2020). Revisit the VEC rule in high entropy alloys (HEAs) with high-throughput CALPHAD approach and its applications for material design-A case study with Al-Co-Cr-Fe-Ni system. *Acta Materialia, 192,* 11-19.

[23] Steurer, W. (2020). Single-phase high-entropy alloys-A critical update. *Materials Characterization, 162,* 110179.

[24] Otto, F., Dlouhy, A., Somsen, C., Bei, H., Eggeler, G., George, E.P. (2013). The influences of temperature and microstructure on the tensile properties of a CoCrFeMnNi high-entropy alloy. *Acta Materialia, 61,* 5743-5755.

[25] Sonkusare, R., Jain, R., Biswas, K., Parameswaran, V., Gurao, N.P. (2020). High strain rate compression behaviour of single phase CoCuFeMnNi high entropy alloy. *Journal of Alloys and Compounds, 823,* 153763.

[26] He, J.Y., Wang, H., Huang, H.L., Xu, X.D., Chen, M.W., Wu, Y., Liu, X.J., Nieh, T.G., An, K., Lu, Z.P. (2016) A precipitation-hardened high-entropy alloy with outstanding tensile properties. *Acta Materialia*, *102*, 187-196.

[27] Zhao, Y.L., Yang, T., Zhu, J.H., Chen, D., Yang, Y., Hu, A., Liu, C.T., Kai, J.-J. (2018). Development of high-strength Co-free high-entropy alloys hardened by nanosize precipitates. *Scripta Materialia*, *148*, 51-55.

[28] Yuan, J.L., Wu, Y.C., Liaw, P.K., Luan, J.H., Jiao, Z.B., Li, J., Han, P.D., Qiao, J.W. (2022). Remarkable cryogenic strengthening and toughening in nano-coherent $CoCrFeNiTi_{0.2}$ high-entropy alloys via energetically-tuning polymorphous precipitates. *Materials Science and Engineering A, 842,* 143111.

[29] Liang, Y.-J., Wang, L., Wen, Y., Cheng, B., Wu, Q., Cao, T., Xiao, Q., Xue, Y., Sha, G., Wang, Y., Ren, Y., Li, X., Wang, L., Wang, F., Cai, H. (2018). High-content ductile coherent nanoprecipitates achieve ultrastrong high-entropy alloys. *Nature Communications, 9*(1), 4063.

[30] Yang, T., Zhao, Y.L., Fan, L., Wei, J., Luan, J.H., Liu, W.H., Wang, C., Jiao, Z.B., Kai, J.J., Liu, C.T. (2020). Control of nanoscale precipitation and elimination of intermediate-temperature embrittlement in multicomponent high-entropy alloys. *Acta Materialia, 189,* 47-59.

[31] Gao, N., Lu, D.H., Zhao, Y.Y., Liu, G.H., Wu, Y., Liu, G., Fan, Z.T., Lu, Z.P., George, E.P. (2019). Strengthening of a CrMnFeCoNi high-entropy alloy by carbide precipitation. *Journal of Alloys and Compounds, 792,* 1028-1035.

[32] Stepanov, N.D., Yurchenko, N.Y., Skibin, D.V., Tikhonovsky, M.A., Salishchev, G.A. (2015). Structure and mechanical properties of the $AlCr_xNbTiV$ (x=0, 0.5, 1, 1.5) high entropy alloys, *Journal of Alloys and Compounds, 652,* 266-280.

[33] Wang, Q., Ma, Y., Jiang, B., Li, X., Shi, Y., Dong, C., Liaw, P.K. (2016). A cuboidal B2 nanoprecipitation-enhanced body-centered-cubic alloy $Al_{0.7}CoCrFe_2Ni$ with prominent tensile properties. *Scripta Materialia, 120,* 85-89.

[34] Peng, J., Li, Z., Fu, L., Ji, X., Pang, Z., Shan, A. (2019). Carbide precipitation strengthening in fine-grained carbon-doped FeCoCrNiMn high entropy alloy. *Journal of Alloys and Compounds, 803,* 491-498.

[35] Dasari, S., Jagetia, A., Chang, Y.-J., Soni, V., Gwalani, B., Gorsse, S., Yeh, A.-C., Banerjee, R. (2020). Engineering multi-scale B2 precipitation in a heterogeeous FCC based microstructure

to enhance the mechanical properties of a $Al_{0.5}Co_{1.5}CrFeNi_{1.5}$ high entropy alloy. *Journal of Alloys and Compounds, 830,* 154707.

[36] He, J.Y., Wang, H., Wu, Y., Liu, X.J., Mao, H.H., Nieh, T.G., Liu, Z.P. (2016). Precipitation behavior and its effects on tensile properties of FeCoNiCr high-entropy alloys. *Intermetallics, 79,* 41-52.

[37] Zhao, Y.Y., Chen, H.W., Lu, Z.P., Nieh, T.G. (2018). Thermal Stability and coarsening of coherent particles in a precipitation-hardened $(NiCoFeCr)_{94}Ti_2Al_4$ high-entropy alloy. *Acta Materialia, 147*, 184-194.

[38] Yang, T., Zhao, Y., Liu, W., Kai, J., Liu, C. (2018). $L1_2$-strengthened high-entropy alloys for advanced structural applications. *Journal of Materials Research, 33(*19), 2983-2997.

[39] Fan, L., Yang, T., Luan, J.H., Jiao, Z.B. (2020). Control of discontinuous and continuous precipitation of γ'-strengthened high-entropy alloys through nanoscale Nb segregation and portioning. *Journal of Alloys and Compounds, 832,* 154903.

[40] Chen, D., He, F., Han, B., Wu, Q., Tong, Y., Zhao, Y., Wang, Z., Wang, J., Kai, J.-J. (2019). Synergistic effect of Ti and Al on L12-phase design in CoCrFeNi-based high entropy alloys. *Intermetallics*, *110*, 106476.

[41] Liu, P.P., Zhao, M.Z., Zhu, Y.M., Bai, J.W., Wan, F.R., Zhan, Q. (2013). Effects of carbide precipitate on the mechanical properties and irradiation behavior of the low activation martensitic steel, *Journal of Alloys and Compounds, 579,* 599-605.

[42] Jin, K., Lu, C., Wang, L.M., Qu, J., Weber, W.J., Zhang, Y., Bei, H. (2016). Effects of compositional complexity on the ion-irradiation induced swelling and hardening in Ni-containing equiatomic alloys. *Scripta Materialia, 119,* 65-70.

[43] He, M.-R., Wang, S., Jin, K., Bei, H., Yasuda, K., Matsumura, S., Higashida, K., Robertson, I.M. (2016). Enhanced damage resistance and novel defect structure of CrFeCoNi under *in situ* electron irradiation. *Scripta Materialia, 125,* 5-9.

[44] Pu, G., Lin, L., Ang, R., Zhang, K., Liu, B., Liu, B., Peng, T., Liu, S., Li, Q. (2020). Outstanding radiation tolerance and mechanical behavior in ultra-fine nanocrystalline $Al_{1.5}$CoCrFeNi high entropy alloy film under He ion irradiation. *Applied Surface Science, 516,* 146129.

[45] Yang, L., Ge, H., Zhang, J., Xiong, T., Jin, Q., Zhou, Y., Shao, X., Zhang, B., Zhu, Z., Zheng, S., Ma, X. (2019). High He-ion irradiation resistance of CrMnFeCoNi high-entropy alloy revealed by comparison study with Ni and 304SS. *Journal of Materials Science and Technology, 35*(3), 300-305.

[46] Li, C., Hu, X., Yang, T., Kumar, N.K., Wirth, B.D., Zinkle, S.J. (2019). Neutron irradiation response of a Co-free high entropy alloy. *Journal of Nuclear Materials, 527,* 151838.

[47] Lu, Y., Huang, H., Gao, X., Ren, C., Gao, J., Zhang, H., Zheng, S., Jin, Q., Zhao, Y., Lu, C., Wang, T., Li, T. (2019). A promising new class of irradiation tolerant materials: $Ti_2ZrHfV_{0.5}Mo_{0.2}$ high-entropy alloy. *Journal of Materials Science and Technology, 35*(3), 369-373.

[48] Yeli, G., Chen, D., Yabuuchi, K., Kimura, A., Liu, S., Lin, W., Zhao, Y., Zhao, S., Kai, J.-J. (2020). The stability of γ' precipitates in a multi-component $FeCoNiCrTi_{0.2}$ alloy under elevated-temperature irradiation. *Journal of Nuclear Materials, 540,* 152364.

[49] Wu, Z., Bei, H. (2015). Microstructures and mechanical properties of compositionally complex Co-free $FeNiMnCr_{18}$ FCC solid solution alloy. *Materials Science and Engineering A*, *640*, 217-224.

[50] Fan, J., Fu, L., Sun, Y., Xu, F., Ding, L., Wen, M., Shan, A. (2022). Unveiling the precipitation behavior and mechanical properties of Co-free $Ni_{47-x}Fe_{30}Cr_{12}Mn_8Al_xTi_3$. *Journal of Materials Science and Technology, 118,* 25-34.

[51] Wu, M., Baker, I. (2020). High strength and high ductility in a novel $Fe_{40.2}Ni_{11.3}Mn_{30}Al_{7.5}Cr_{11}$ multiphase high entropy alloy. *Journal of Alloys and Compounds, 820,* 153181.

[52] Wang, L., Wang, L., Zhou, S., Xiao, Q., Xiao, Y., Wang, X., Cao, T., Ren, Y., Liang, Y.-J., Wang, L., Xue, Y. (2021). Precipitation and micromechanical behavior of the coherent ordered nanoprecipitation strengthened Al-Cr-Fe-Ni-V high entropy alloy. *Acta Materialia, 216*, 117121.

[53] Chen, S.-T., Tang, W.-Y., Kuo, Y.-F., Chen, S.-Y., Tsau, C.-H., Shun, T.-T., Yeh, J.-W. (2010). Microstructure and properties of age-hardnable $Al_xCrFe_{1.5}MnNi_{0.5}$ alloys. *Materials Science and Engineering A, 527,* 5818-5825.

[54] Zhang, M., Zhang, L., Fan, J., Yu, P., Li, G. (2019). Novel Co-free $CrFeNiNb_{0.1}Ti_x$ with ultra high hardness and strength. *Materials Science and Engineering A, 764,* 138212.

[55] Lu, W., Luo, X., Yang, Y., Le, W., Huang, B., Li, P. (2020). Co-free non-equilibrium medium-entropy alloy with outstanding tensile properties. *Journal of Alloys and Compounds, 833,* 155074

[56] Thompson, K., Lawrence, D., Larson, D.J., Olson, J.D., Kelly, T.F., Gorman, B. (2007). In situ site-specific specimen preparation for atom probe tomography. *Ultramicroscopy*, *107*(2-3), 131-139.

[57] Ilavsky, J., Zhang, F., Andrews, R.N., Kuzmenko, I., Jemian, L.E., Allen, A.J. (2018). Development of combined microstructure and structure characterization facility for in situ and operando studies at the advanced photon source, *Journal of Applied Crystallography, 51*(3), 867-882.

[58] Ruett, U., Almer, J., Kenesei, P., Park, J.-S., Osborn, R., Ren, Y., Robinson, D., Krogstad, M., Rosenkranz, S., Zhang, X. (2020). High-energy x-rays expediting applied and fundamental research, *Synchrotron Radiation News, 33*(6), 44-50.

[59] Makhlouf, S.A., Nakamura, T., Shiga, M. (1994). Structure and magnetic properties of $FeAl_{1-x}Rh_x$ alloys. *Journal of Magnetism and Magnetic Materials, 135,* 257-264.

[60] Yu, P.F., Cheng, H., Zhang, L.J., Zhang, H., Ma, M.Z., Li, G., LIaw, P.K., Liu, R.P. (2016). Nanotwin's formation and growth in an AlCoCuFeNi high-entropy alloy, *Scripta Materialia, 114,* 31-34.

[61] Lee, T.-H., Kim, S.-J., Jung, Y.-C. (2000). Crystallographic Details of Precipitates in Fe-22Cr-21Ni-6Mo-(N) Superaustenitic Stainless Steels Aged at 900 °C. *Metallurgical and Materials Transactions A, 31A,* 1713-1723.

[62] Qu, P., Yang, W., Qin, J., Liu, C., Cao, K., Zhang, J., & Liu, L. (2020). Precipitation behavior and chemical composition of secondary γ' precipitates in a Re-containing Ni-based single crystal superalloy. *Intermetallics*, *119*, 106725.

[63] Chang, Y-J. and Yeh, A-C.: The evolution of microstructures and high temperature properties of AlxCo$_{1.5}$CrFeNi$_{1.5}$Tiy high entropy alloys. *J. Alloys Compd.* 653, 379 (2015)

[64] Tsao, T-K., Yeh, A-C., and Murakami, H. (2017). The microstructure stability of precipitation strengthened medium to high entropy superalloys**.** *Metall. Mater. Trans. A* 48, 2435

[65] Fahrmann, M.G., and Metzler, D.A. (2016). Simulation of γ' Precipitation Kinetics in a Commercial Ni-Base Superalloy, *Journal of Materials, 68*(11), 2786-2792.

[66] Bonvalet, M., Philippe, T., Sauvage, X., Blavette, D. (2015). Modeling of precipitation kinetics in multicomponent systems: Application to model superalloys, *Acta Materialia, 100,* 169-177.

[67] Rafiei, M., Mirzadeh, H., Malekan, M. (2019). Micro-mechanisms and precipitation kinetics of delta (δ) phase in Inconel 718 superalloy during aging, *Journal of Alloys and Compounds, 795,* 207-212.

[68] Wang, S., Zhao, Y., Xu, X., Cheng, P., Hou, H. (2020). Evolution of mechanical properties and corrosion resistance of $Al_{0.6}CoFeNiCr_{0.4}$ high-entropy alloys at different heat treatment temperature, *Materials Chemistry and Physics, 244,* 122700.

[69] Li, L., Li, Z., da Silva, A.K., Peng, Z., Zhao, H., Gault, B., Raabe, D. (2019). Segregation-driven grain boundary spinodal decomposition as a pathway for phase nucleation in a high-entropy alloy, *Acta Materialia, 178,* 1-9.

[70] Soni, V., Gwalani, B., Alam, T., Dasari, S., Zheng, Y., Senkov, O.N., Miracle, D., Banerjee, R. (2020). Phase inversion in a two-phase, BCC+B2, refractory high entropy alloy, *Acta Materialia, 185,* 89-97.

[71] Zhang, Y., Chen, Z., Cao, D., Zhang, J., Zhang, P., Tao, Q., Yang, X. (2019). Concurrence of spinodal decomposition and nano-phase precipitation in a multi-component AlCoCrCuFeNi high-entropy alloy, *Journal of Materials Research and Technology, 8(1),* 726-736.

[72] Villanueva, D.M.E., Junior, F.C.P. Plaut, R.L., and Padilha, A.F. (2006). Comparative study on sigma phase precipitation of three types of stainless steels: austenitic, superferritic and duplex. *Materials Science and Technology, 22*(9), 1098-1104.

[73] Pohl, M., Storz, O., Glogowski, T. (2007). Effect of intermetallic precipitations on the properties of duplex stainless steel. *Materials Characterization, 58*(1), 65-71.

[74] Cho, H.-S., Lee, K. (2013). Effect of cold working and isothermal aging on the precipitation of sigma phase in 2205 duplex stainless steel. *Materials Characterization, 75,* 29-34.

[75] Magnabosco, R. (2009). Kinetics of sigma phase formation in a Duplex Stainless Steel. *Materials Research, 12*(3), 321-327.

[76] Gwalani, B., Ayyagari, A.V., Choudhari, D., Scharf, T., Mukharjee, S., Gibson, M., Banerjee, R. (2018). Microstructure and wear resistance of an intermetallic-based Al0.25Ti0.75CoCrFeNi high entropy alloy. *Materials Chemistry and Physics, 210,* 197-206.

[77] Cieslak, M. J., Ritter, A. M., Savage, W. F. (1984). Chi-phase formation during solidification and cooling of CF-8 M weld metal. *Welding Journal*, *63*(4), 133.

[78] Xu, W., San Martin, D., Del Castillo, P. R. D., Van der Zwaag, S. (2007). Modelling and characterization of chi-phase grain boundary precipitation during aging of Fe–Cr–Ni–Mo stainless steel. *Materials Science and Engineering: A*, *467*(1-2), 24-32.

[79] Okafor, I.C.I., Carlson, O.N. (1978). Equilibrium Studies on a Chi Phase-Strengthened Ferritic Alloy. *Metallurgical Transactions A, 9A,* 1651-1657.

[80] Jeon, S.-H., Kim, H.-J., Park, Y.-S. (2014). Effects of inclusions on the precipitation of chi phases and intergranular corrosion resistance of hyper duplex stainless steel. *Corrosion Science, 87,* 1-5.

[81] Escriba, D.M., Materna-Morris, E., Plaut, R.L., Padilha, A.F. (2009). Chi-phase precipitation in a duplex stainless steel. *Materials Characterization*, *60*(11), 1214-1219.

[82] Ghosh, S.K, Mondal, S. (2008). High temperature ageing behaviour of a duplex stainless steel. *Materials Characterization, 59,* 1776-1783

[83] Tsai, M.-H., Chang, K.-C., Li, J.-H., Tsai, R.-C., Cheng, A.-H. (2016). A second criterion for sigma phase formation in high-entropy alloys. *Materials Research Letters, 4*(2), 90-95.

[84] Wen, H., Topping, T. D., Isheim, D., Seidman, D. N., & Lavernia, E. J. (2013). Strengthening mechanisms in a high-strength bulk nanostructured Cu–Zn–Al alloy processed via cryomilling and spark plasma sintering. *Acta Materialia*, *61*(8), 2769–2782.

[85] Booth-Morrison, C., Dunand, D.C., Seidman, D.N. (2011). Coarsening Resistance at 400°C of precipitation-strengthened Al-Zr-Sc-Er alloys. *Acta Materialia*, *59,* 7029-7042

[86] Yasuda, H., Takasugi, T., Koiwa, M. (1992). Elasticity of Ni-based $L1_2$-type intermetallic compounds. *Acta Metallurgica et Materialia, 40*(2), 381-387.

[87] Argon, A.S., Pollock, T.M. (1992). Creep resistance of CMSX-3 nickel base superalloy single crystals. *Acta Materialia, 40*, 1-30.

[88] Pommeranke, H., Duan, J., Curtis, N., DeLibera, V., Bratten, A., Hoffman, A., Buchely, M., O'Malley, R., Wen, H. (2023). A strong and ductile cobalt-free solid-solution $Fe_{30}Ni_{30}Mn_{30}Cr_{10}$ multi-principal element alloy from hot rolling. *Journal of Alloys and Compounds, 948,* 169566.

[89] Dey, G. K., & Sekhar, J. A. (1997). Micropyretic synthesis of tough NiAl alloys. *Metallurgical and Materials Transactions B, 28*(5), 905-918.

Figures

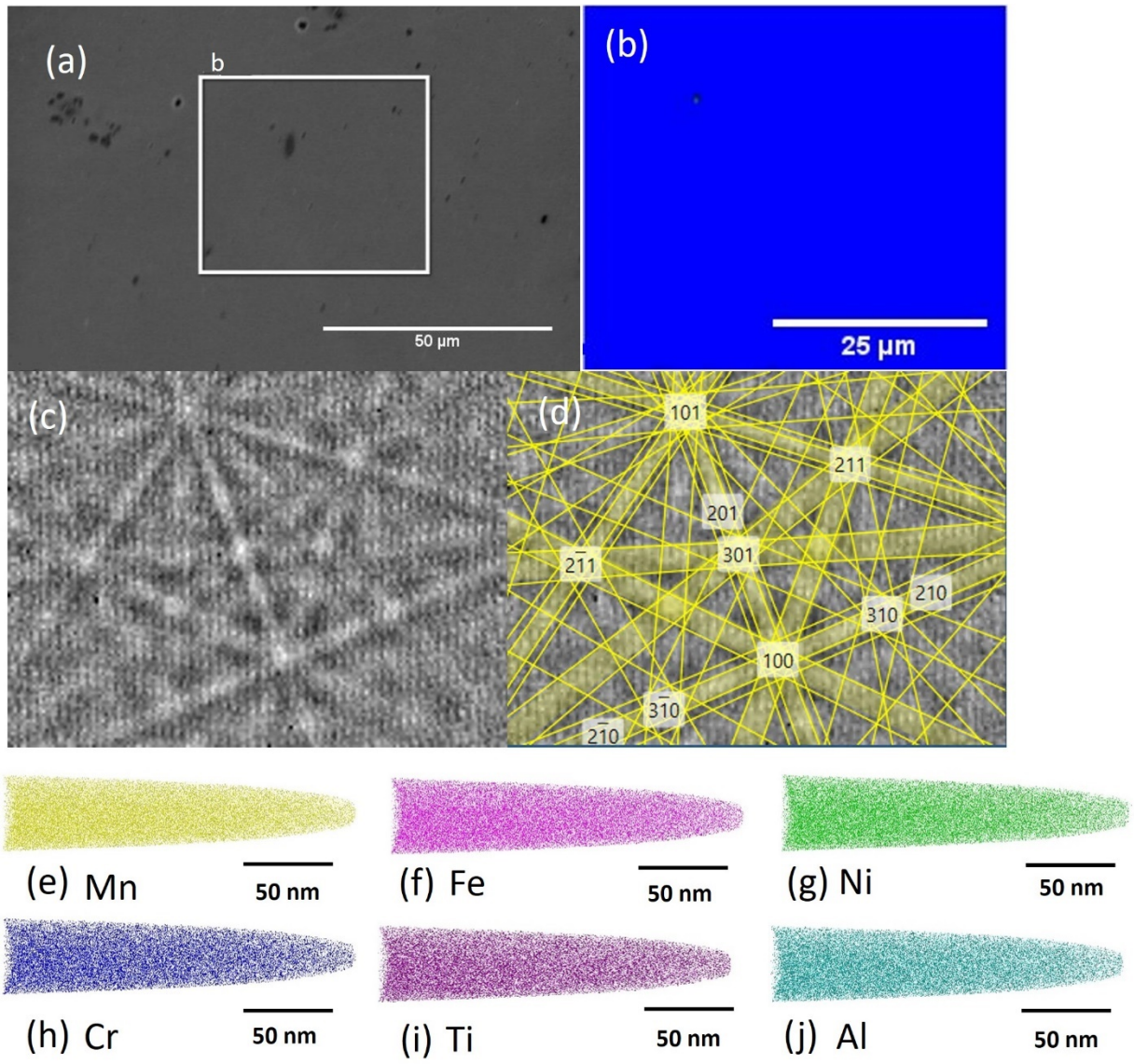

Figure 1: $(Fe_{0.3}Ni_{0.3}Mn_{0.3}Cr_{0.1})_{88}Ti_4Al_8$ homogenized at 1100 °C for 48 hours. (a) Secondary electron SEM image; (b) EBSD phase map of homogenized sample, blue corresponding to FCC iron; (c) Unindexed Kikuchi pattern and (d) indexed Kikuchi diffraction pattern (FCC). APT reconstruction atom maps of (e) Mn, (f) Fe, (g) Ni, (h) Cr, (i) Ti and (j) Al indicate compositional homogeneity.

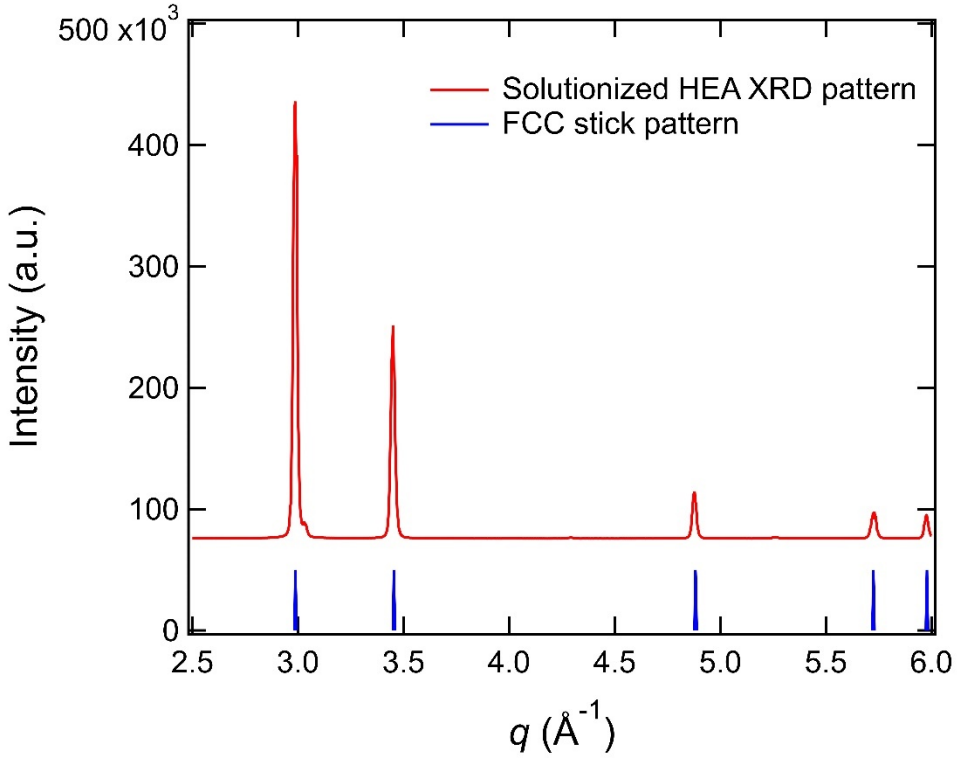

Figure 2: Synchrotron XRD pattern of $(Fe_{0.3}Ni_{0.3}Mn_{0.3}Cr_{0.1})_{88}Ti_4Al_8$ homogenized at 1100 °C for 48 hours. The pattern closely matches an FCC pattern with a lattice parameter of (3.640 ± 0.002) Å

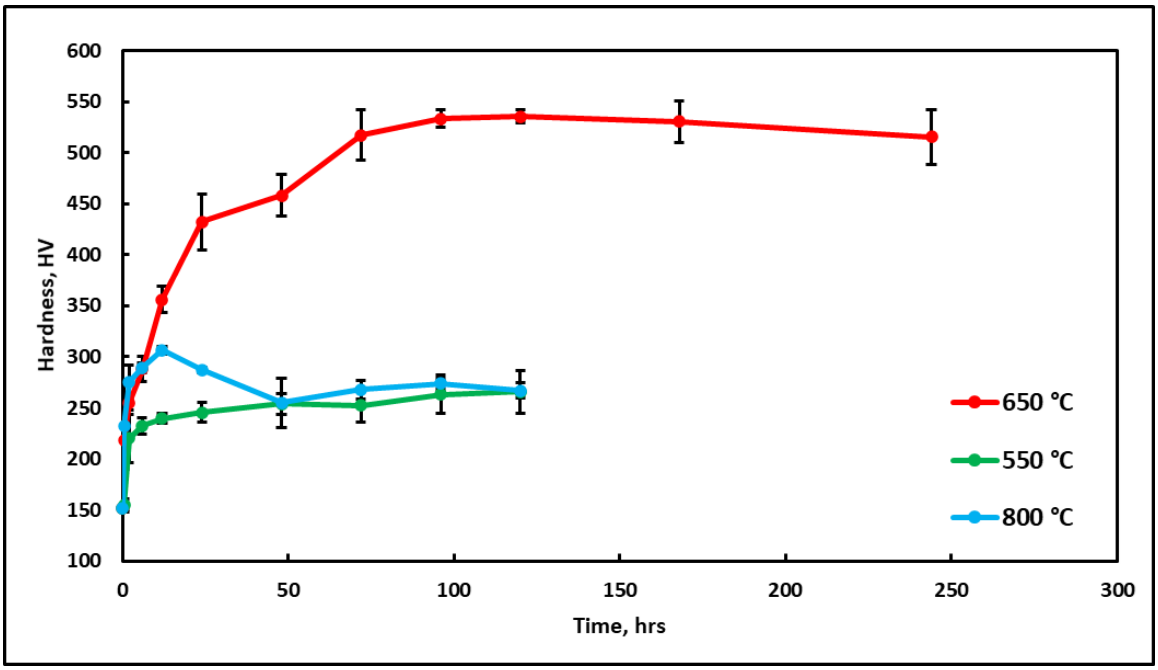

Figure 3. Vickers microhardness of $(Fe_{0.3}Ni_{0.3}Mn_{0.3}Cr_{0.1})_{88}Ti_4Al_8$ aged at 550 °C, 650 °C, and 800 °C after homogenization.

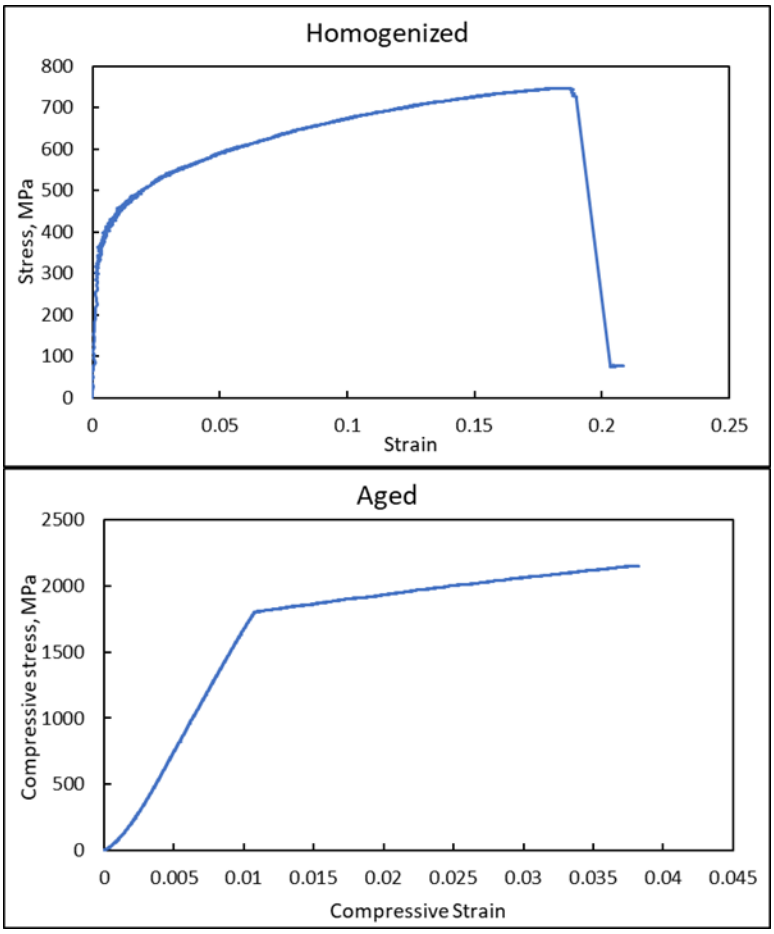

Figure 4: Mechanical properties of $(Fe_{0.3}Ni_{0.3}Mn_{0.3}Cr_{0.1})_{88}Ti_4Al_8$ in as-homogenized state (tensile data) and aged at 650 °C for 120 hours (compressive data)

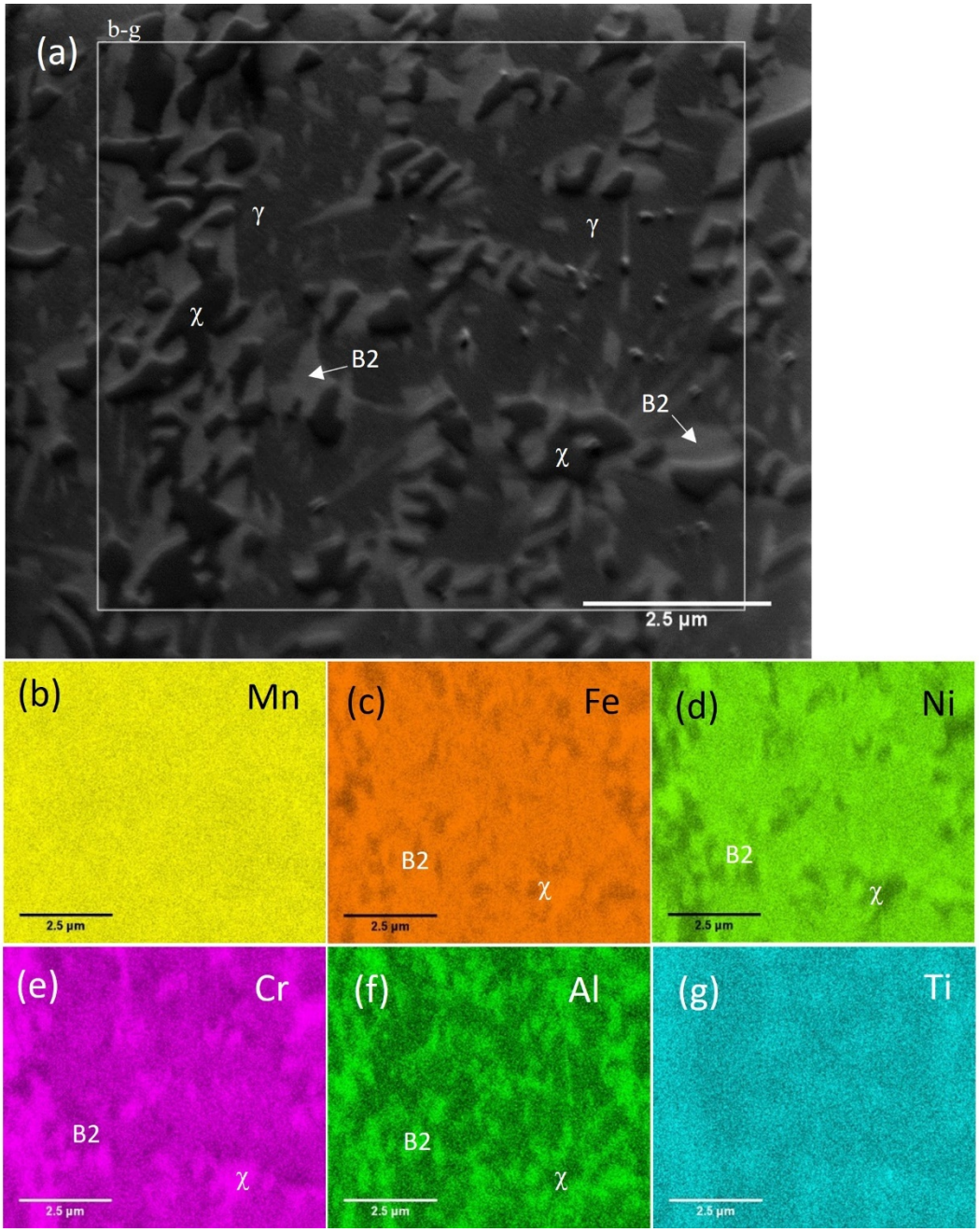

Figure 5: Secondary electron SEM image and EDS elemental maps of $(Fe_{0.3}Ni_{0.3}Mn_{0.3}Cr_{0.1})_{88}Ti_4Al_8$ aged at 650 °C for 120 h. (a) Secondary electron image; (b) Mn; (c) Fe; (d) Ni; (e) Cr; (f) Al; and (g) Ti EDS elemental maps. Examples of B2 and χ phases forming in the matrix are labeled.

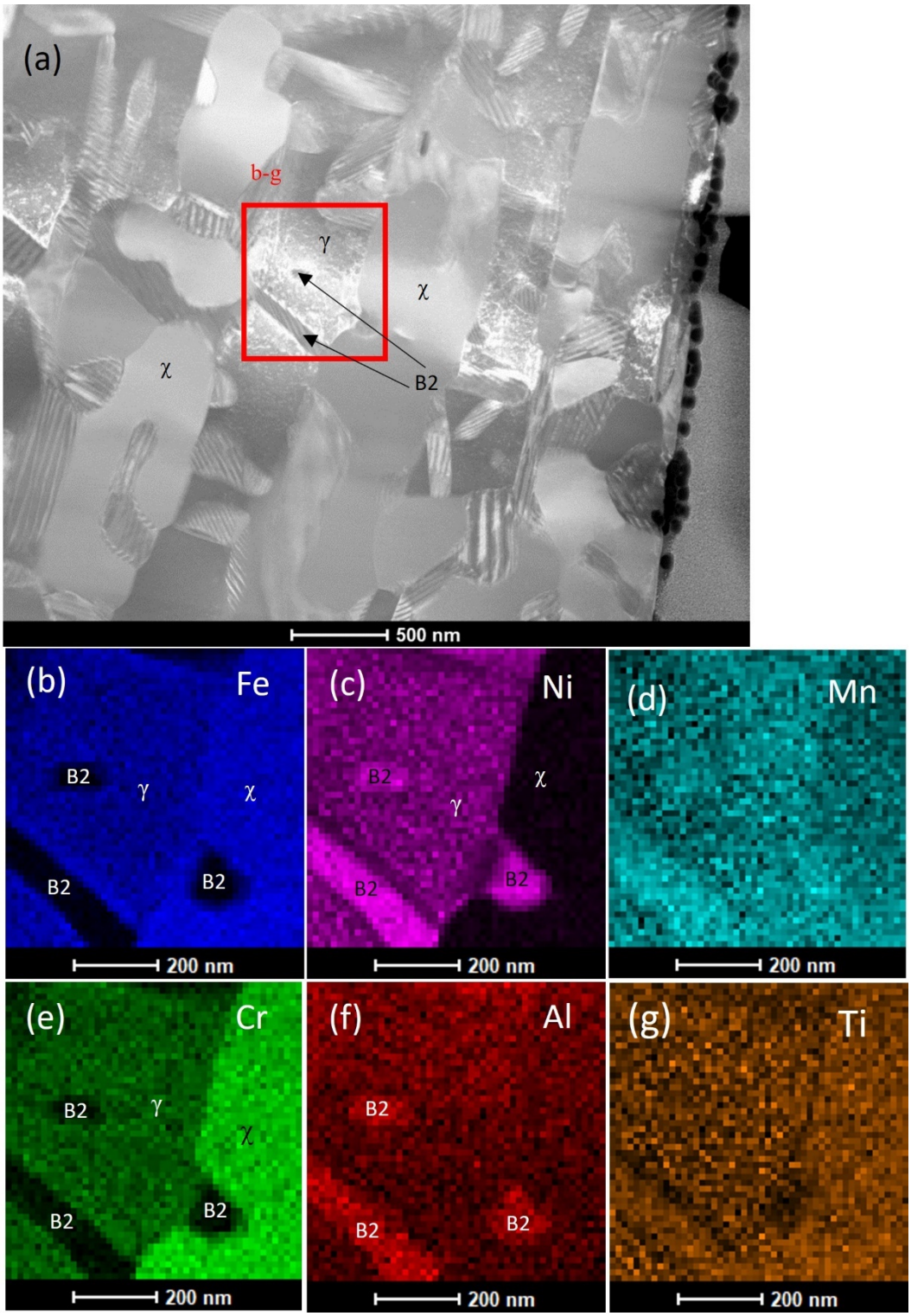

Figure 6: Scanning transmission electron microscopy (STEM) of $(Fe_{0.3}Ni_{0.3}Mn_{0.3}Cr_{0.1})_{88}Ti_4Al_8$ aged at 650 °C for 120 h with elemental maps. (a) Bright field STEM; (b) Fe; (c) Ni; (d) Mn; (e) Cr; (f) Al; and (g) Ti EDS elemental maps. FeCr and NiAl rich phases are labeled as χ and B2, respectively.

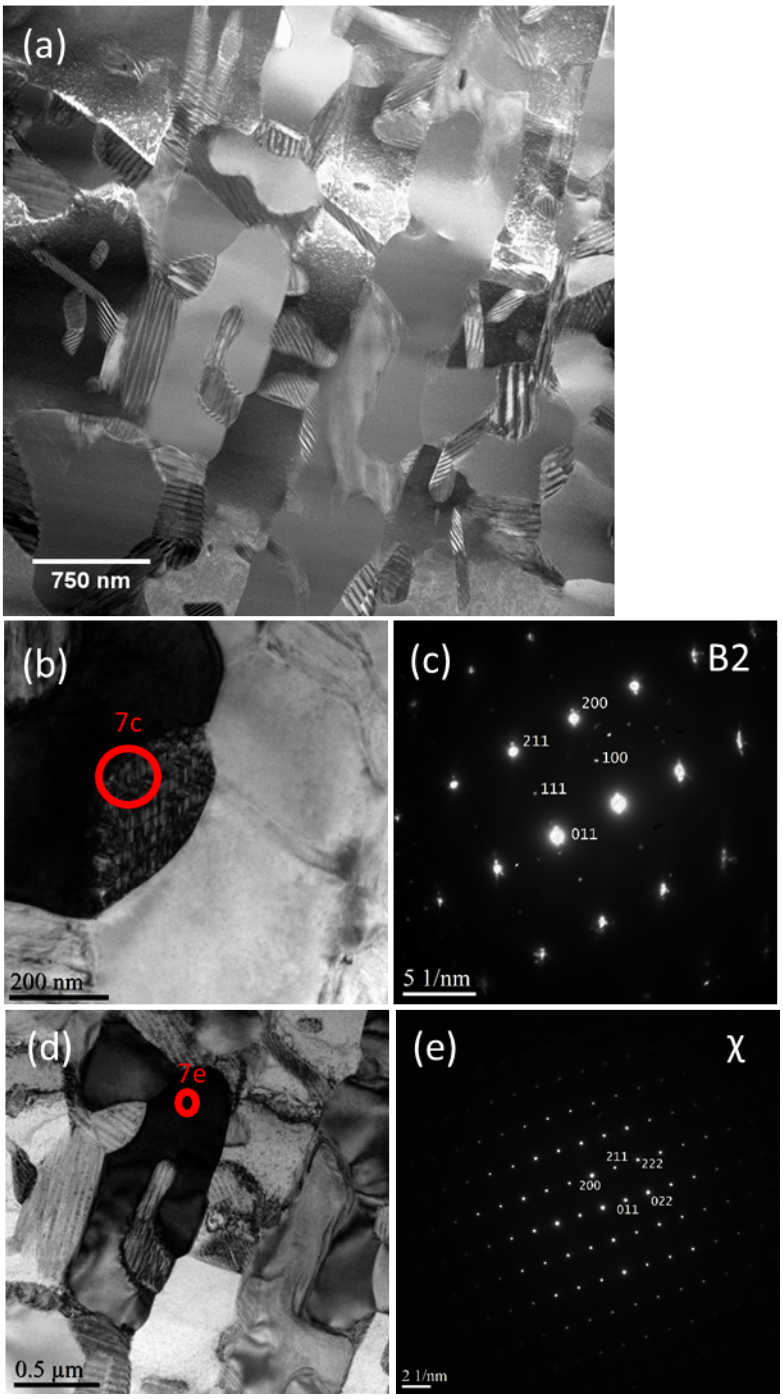

Figure 7: TEM of $(Fe_{0.3}Ni_{0.3}Mn_{0.3}Cr_{0.1})_{88}Ti_4Al_8$ aged at 650 °C for 120 h showing closely coupled B2 and χ phases. (a) Bright-field STEM image; (b) Bright-field TEM image of a B2 phase particle; (c) Selected-area electron diffraction (SAED) pattern of (b) confirming that the particle is B2 phase; (d) Bright-field TEM of a χ phase particle; (e) SAED of (d) confirming that the particle is χ phase.

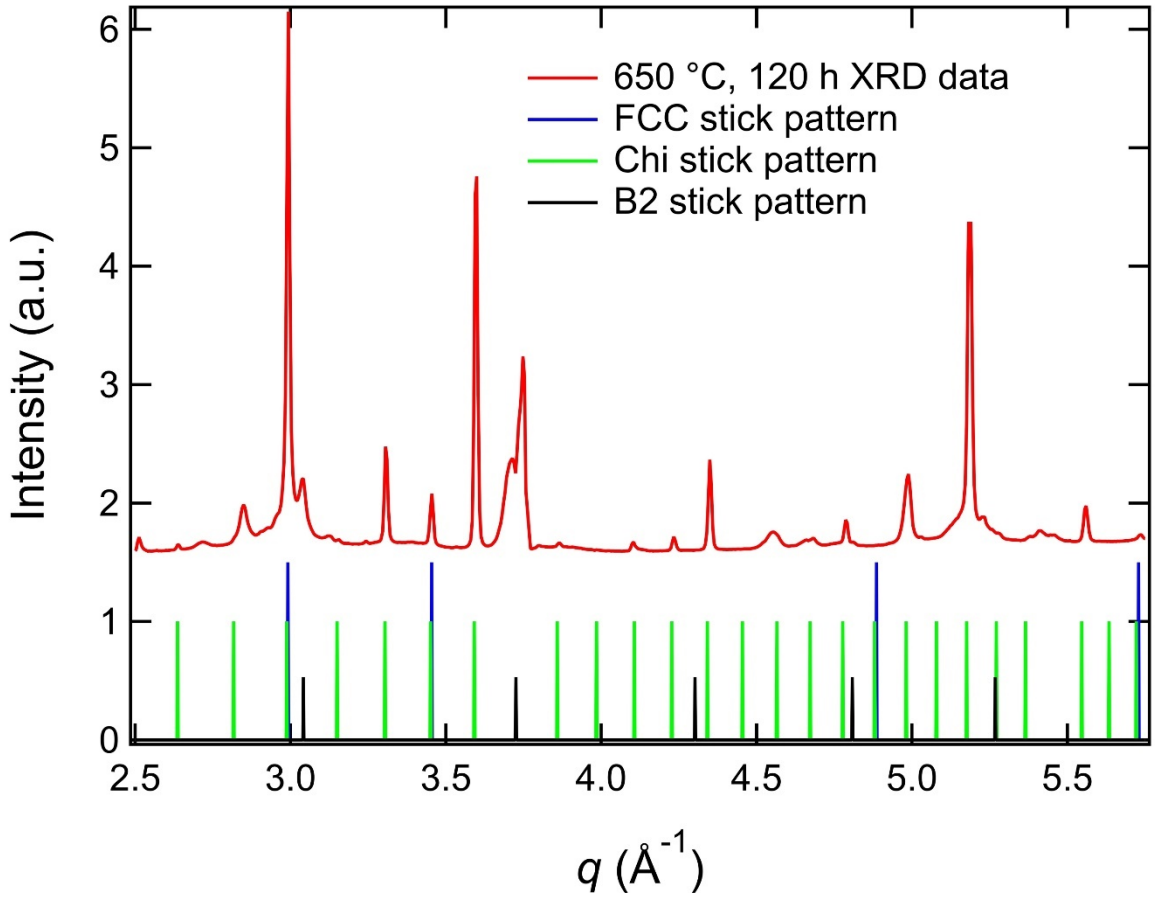

Figure 8: Bulk XRD data of $(Fe_{0.3}Ni_{0.3}Mn_{0.3}Cr_{0.1})_{88}Ti_4Al_8$ aged at 650 °C for 120 h and simulated stick patterns of the FCC matrix (a = 3.638 Å), B2 phase (a = 2.922 Å) and χ(Chi) phase (I -4 3 m symmetry, a = 8.892 Å). The FCC lattice parameter of the aged specimen is slightly smaller than that of the homogenized alloy (3.640 Å), suggesting that the FCC matrix has a similar composition before and after the aging. The lattice parameters determined for B2 and χ are similar to those in the literature, but very slightly different from those measured from TEM.

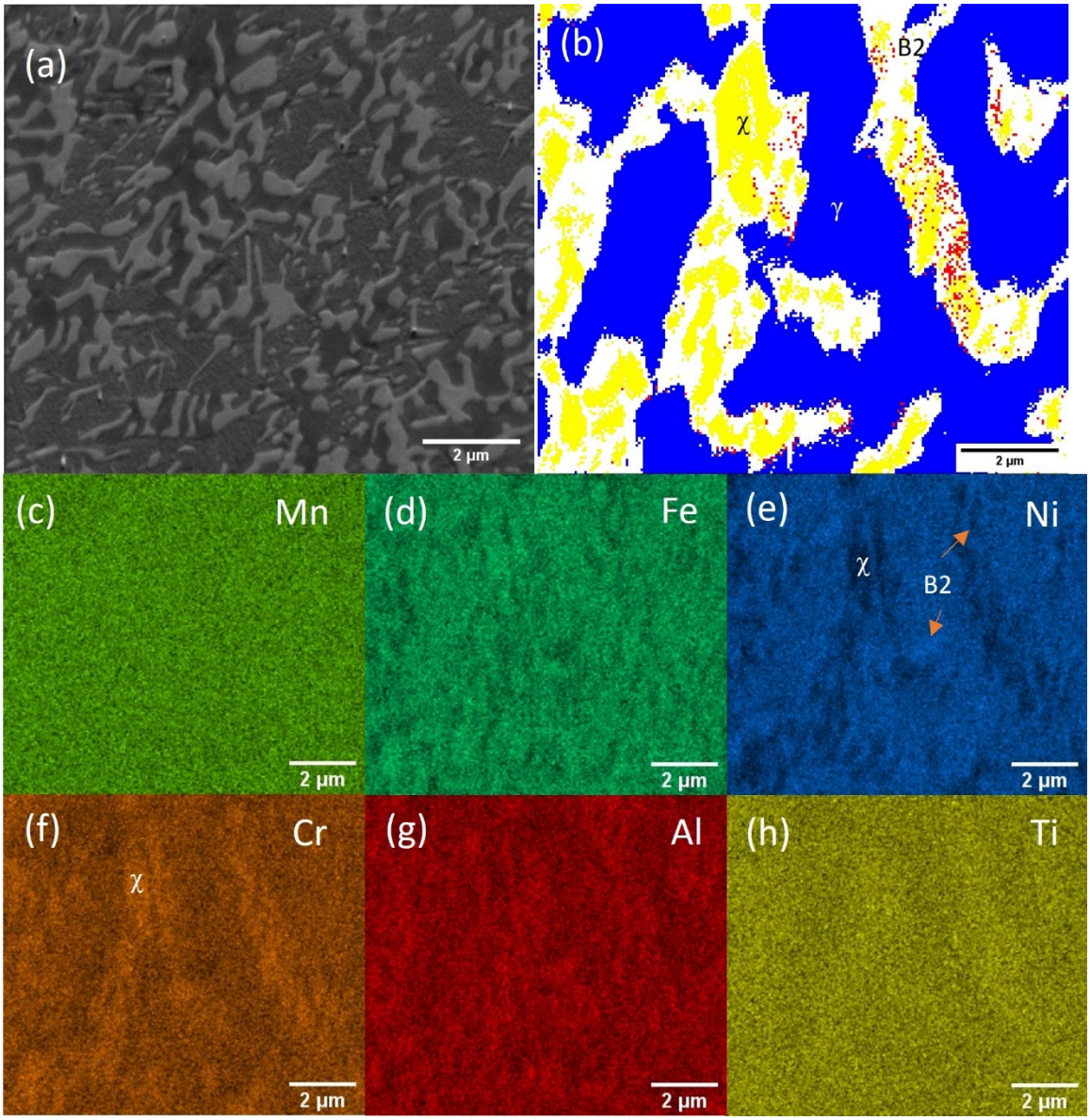

Figure 9: EBSD map of $(Fe_{0.3}Ni_{0.3}Mn_{0.3}Cr_{0.1})_{88}Ti_4Al_8$ aged at 650 °C for 120 h indexing the Cr-rich phase as χ phase, while B2 phase did not index clearly. (a) Electron image; (b) Phase map, blue=fcc, red=B2, yellow=χ; EDS maps of (c) Mn, (d) Fe, (e) Ni, (f) Cr, (g) Al, (h) Ti.

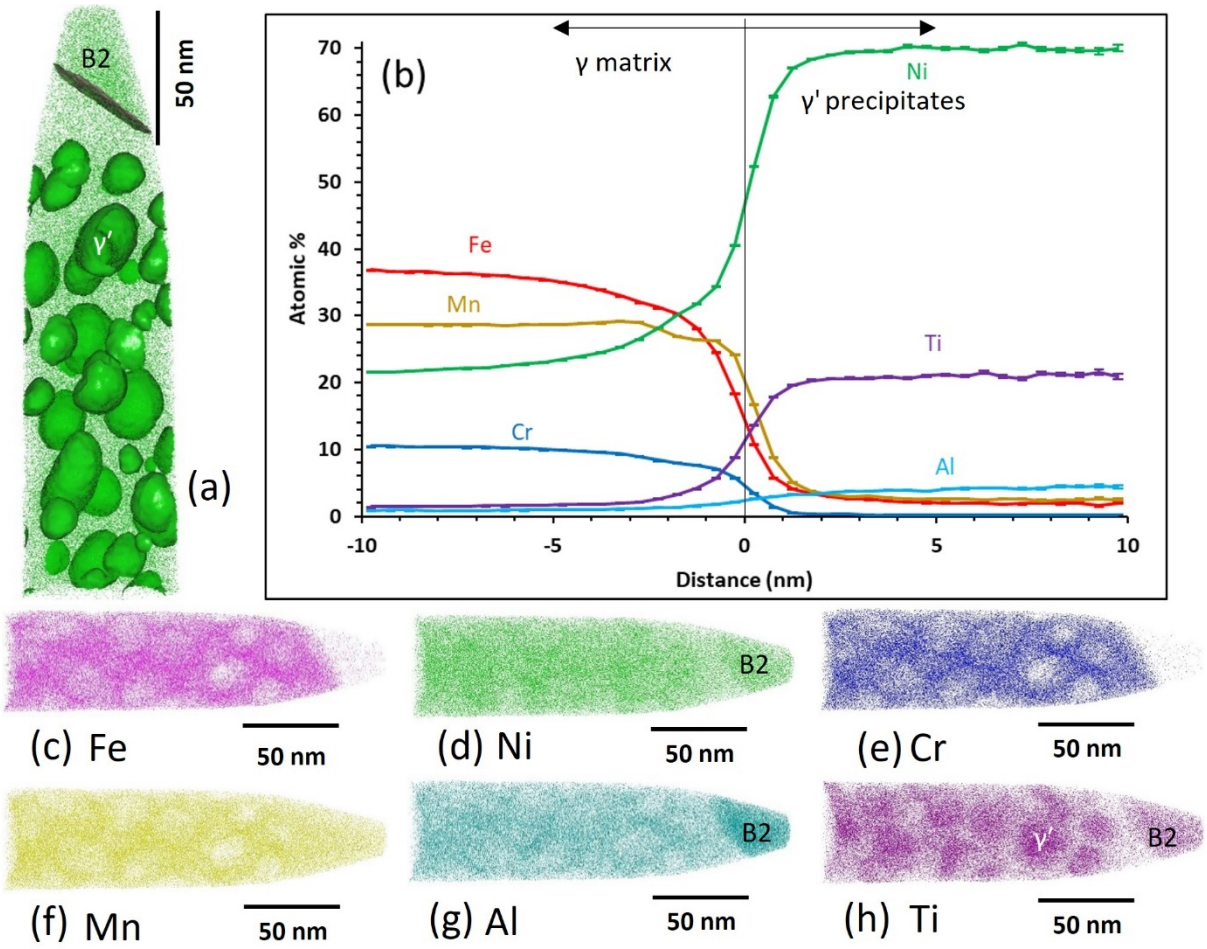

Figure 10: APT reconstruction of $(Fe_{0.3}Ni_{0.3}Mn_{0.3}Cr_{0.1})_{88}Ti_4Al_8$ aged at 650 °C for 120 h. (a) 40% Ni iso-concentration surface delineating γ′ precipitates, with Ni atoms superimposed; (b) proximity histogram of the γ′ precipitates, showing their average concentration profile; atom maps of (c) Fe, (d) Ni, (e) Cr, (f) Mn, (g) Al, and (h) Ti. The γ′ phase is labeled in white, while the B2 phase is labeled in black.

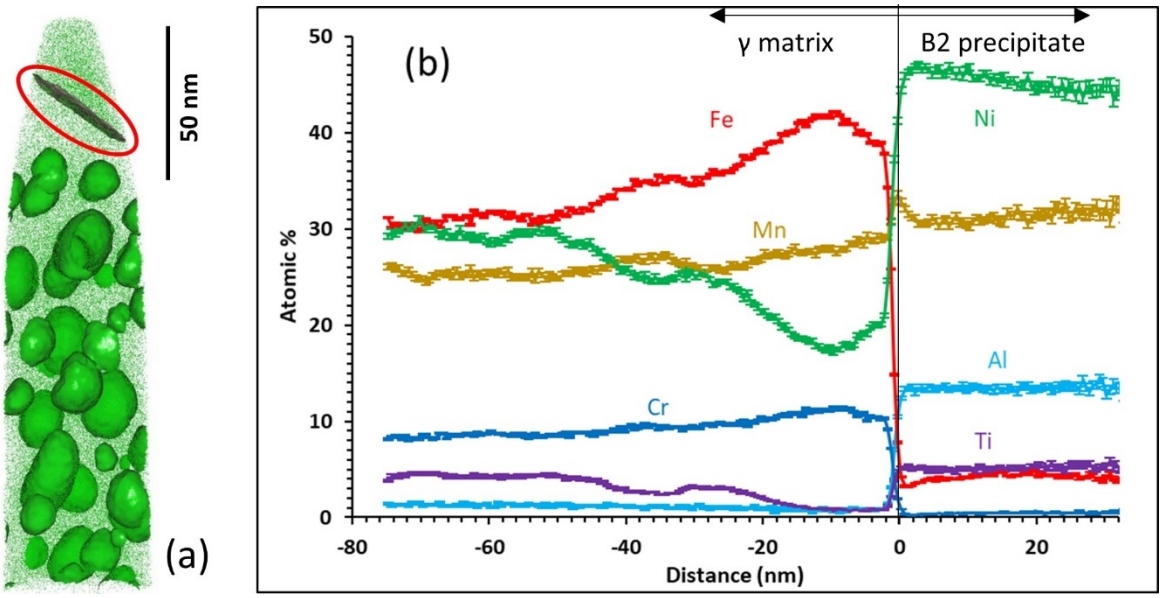

Figure 11: The same APT dataset shown in Figure 10 with a B2 precipitate composition profile: (a) a 40 at.% Ni iso-concentration surface (circled) delineating the interface between the γ matrix and B2 precipitate; (b) proxigram concentration profile based on the 40 at.% Ni iso-concentration surface shown in (a). Note that the B2 particle is located at the top of the APT tip, and the tip only includes part of the particle.

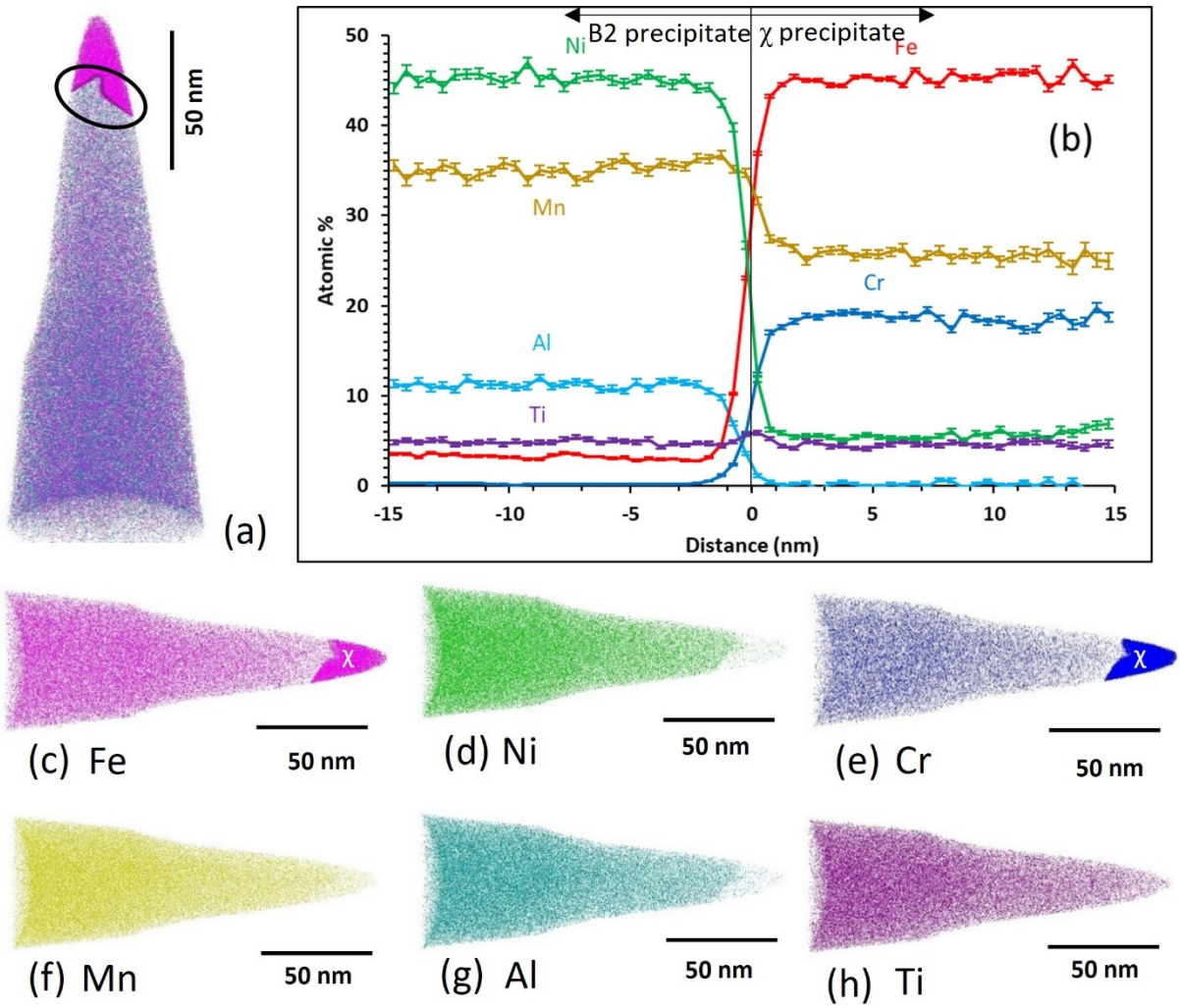

Figure 12: APT data for $(Fe_{0.3}Ni_{0.3}Mn_{0.3}Cr_{0.1})_{88}Ti_4Al_8$ aged at 650 °C for 120 h showing a FeCr-rich χ phase joining a B2 precipitate. (a) A 25 at.% Fe iso-concentration surface (circled) used for the proxigram shown in (b) proxigram; atom maps of (c) Fe, (d) Ni, (e) Cr, (f) Mn, (g) Al, and (h) Ti. The Fe and Cr enrichment of the χ phase is indicated with labels.

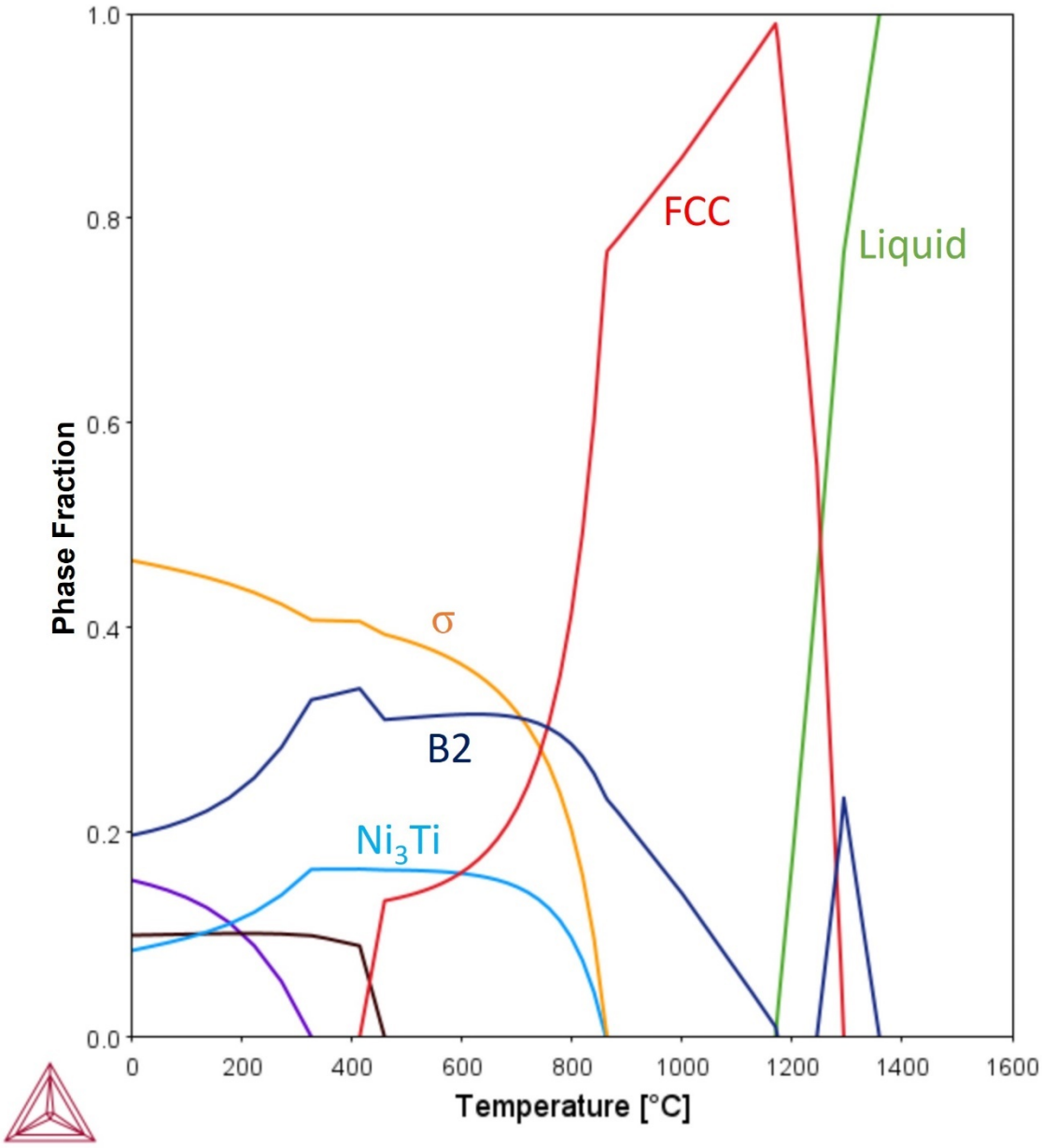

Figure 13: CALPHAD predictions of equilibrium phase formation. Phases relevant to 650 °C aging are labeled.

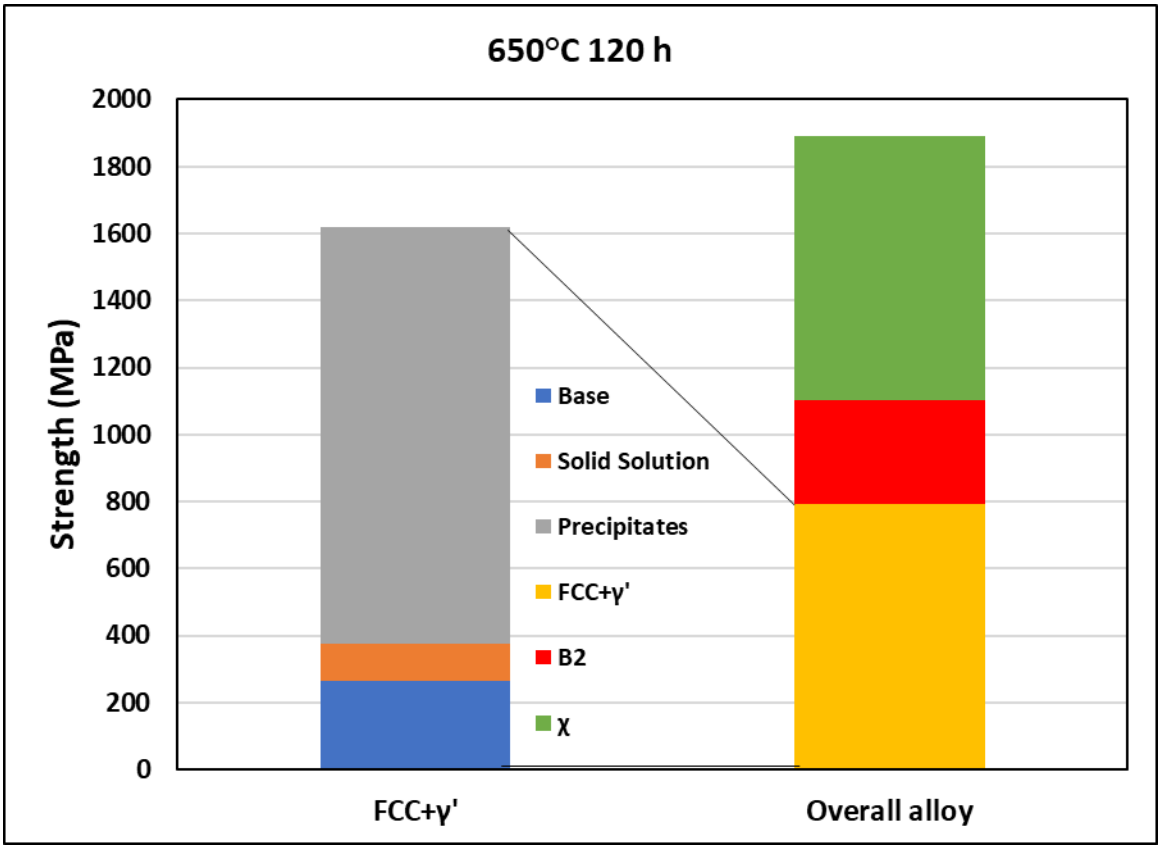

Figure 14: Strengthening analysis of the peak aged sample. The left column illustrates the strengthening mechanisms of the FCC+γ′ section of the alloy. The right column uses the load transfer strengthening equation to determine the overall strength of the alloy, using the left column as an input to account for the strengthening from the FCC+γ′ section of the alloy. The yellow part of the right column is equal to the volume percentage (48.91%) of the FCC+γ′ section multiplied by the overall height of the left column.